Constraints on Resonant Dark Matter Annihilation

By

Mihailo Backović

Submitted to the Department of Physics and Astronomy and the
Faculty of the Graduate School of the University of Kansas
in partial fulfillment of the requirements for the degree of

Doctor of Philosophy

John P. Ralston, Chair

Douglas W. McKay

Committee members

Kyoungchul Kong

Hume A. Feldman

David E. Lerner

Date defended:

The Dissertation Committee for Mihailo Backović certifies
that this is the approved version of the following dissertation:

Constraints on Resonant Dark Matter Annihilation

Committee:

John P. Ralston, Chair

Douglas W. McKay

Kyoungchul Kong

Hume A. Feldman

David E. Lerner

Date approved:

Abstract

Resonant dark matter annihilation drew much attention in the light of recent measurements of charged cosmic ray fluxes. Interpreting the anomalous signal in the positron fraction as a sign of dark matter annihilation in the galactic halo requires cross sections orders of magnitudes higher than the estimates coming from thermal relic abundance. Resonant dark matter annihilation provides a mechanism to bridge the apparent contradiction between thermal relic abundance and the positron data measured by PAMELA and FERMI satellites.

In this thesis, we analyze a class of models which allow for dark matter to annihilate through an s-channel resonance. Our analysis takes into account constraints from thermal relic abundance and the recent measurements of charged lepton cosmic ray fluxes, first separately and then simultaneously.

Consistency of resonant dark matter annihilation models with thermal relic abundance as measured by WMAP serves to construct a relationship between the full set of masses, couplings and widths involved. Extensive numerical analysis of the full four dimensional parameter space is summarized by simple analytic approximations. The expressions are robust enough to be generalized to models including additional annihilation channels.

We provide a separate treatment of resonant annihilation of dark matter in the galactic halo. We find model-independent upper limits on halo dark matter annihilation rates

and show that the most efficient annihilation mechanism involves s-channel resonances. Widths that are large compared to the energy spread in the galactic halo are capable of saturating unitarity bounds without much difficulty. Partial wave unitarity prevents the so called Sommerfeld factors from producing large changes in cross sections. In addition, the approximations made in Sommerfeld factors break down in the kinematic regions where large cross section enhancements are often cited.

Simultaneous constraints from thermal relic abundance and halo annihilation serve to produce new limits on dark matter masses and couplings. Past considerations of only a part of the resonant annihilation parameter set to motivate large annihilation cross section enhancements in the halo while maintaining correct relic abundance are generally incomplete. Taking into account only the resonance mass and width to show that large cross section enhancements are possible does not in principle guarantee that the enhancement will be achieved. We extend the calculation to include the full resonant parameter set. As a result, we obtain new limits on dark matter masses and couplings.

Contents

List of Figures

List of Tables

Chapter 1

Introduction

1.1 Brief History of Dark Matter

Existence of dark matter was proposed nearly half a century ago as an explanation for the anomalous behavior of the galaxy rotation curves [1–3]. To date, no experiment has been able to directly observe dark matter, although indirect evidence such as large structure formation and gravitational lensing in the backgrounds of galaxy clusters offer hints of its existence.

Other than knowing that dark matter must couple to gravity, the true nature of dark matter interactions at particle physics scales remains largely unknown. The Standard Model of particle physics describes three generations of matter and their interactions through electro-magnetic, weak and strong forces, while gravity has not yet been successfully implemented. A tremendous amount of experimental data has been explained by the Standard Model to a very high level of accuracy. Yet, despite its enormous success, the Standard Model does not contain a dark matter candidate capable of accommodating all astro-physical and cosmological data [1]. For the last few decades, this

[1] Neutrinos could constitute a fraction of dark matter, but cannot account for the entire dark matter content as estimated by the Wilkinson Microwave Anisotropy Probe (WMAP) [4].

fact has driven the massive experimental and theoretical effort to discover particle dark matter.

With the discovery of the anisotropies in the cosmic microwave background (CMB), cosmology has become an active experimental field. Given a model of the universe, the CMB anisotropies can be mapped into cosmological parameters, one of them being the relic density of dark matter. WMAP [4] estimates dark matter to provide $\sim 25\%$ of the energy content of the universe in the context of the Standard Cosmological Model.

At present, a diverse spectrum of experimental dark matter searches is underway. Direct dark matter detection experiments such as CDMS [5], DAMA/LIBRA, DAMA / NaI [6], COGENT [7] and XENON100 [8, 9] are looking for signals of possible interactions of galactic halo dark matter with atomic nuclei. Both XENON100 and CDMS have recently claimed events in the dark matter signal region. However, at this point it is hard to determine whether the observed events are truly dark matter due to very low statistics. COGENT has claimed a statistically significant excess of events in the low energy nuclear recoil region. Uncertainties about the nature of backgrounds and their levels in the COGENT signal region make it difficult to confirm that the excess is truly due to dark matter interactions. For some time now, DAMA has observed an annual modulation in the event rate. The group attributes the signal to the annual changes in the flux of dark matter as the Earth moves around the Sun. Meanwhile, many backgrounds relevant to DAMA show annual modulations in phase with the signal [10].

Dark matter could in principle be produced in collider experiments. The Large Hadron Collider (LHC) will search for possible signals of dark matter produced in ultra-high energy proton proton collisions.

Earth based indirect detection experiments, such as AMANDA [11], IceCube [12, 13] and ANTARES [14] are searching for neutrino signals coming from dark matter annihilation in the Sun or the Earth. At this time, no signal has been reported. Satellite

based indirect detection experiments PAMELA [15], FERMI [16] and PPB-BETS [17] suggested a significant signal in excess positron production in galactic halos, as long suggested by the HEAT [18] and ATIC [19] experiments. Possible explanations range from exotic mechanisms [20, 21], uncertain features of pulsars [22–25], to dark matter decays [26–28] and dark matter annihilation [29–34]. FERMI is also looking for dark matter signatures in the diffuse gamma ray fluxes. So far, no significant excess has been reported [35].

Much of our work in this thesis is focused on recent results from PAMELA and FERMI. We will discuss these results in much more detail in Chapter 5.

1.2 Resonant Annihilation of Dark Matter - Motivation and Outline

The excess in the positron fraction relative to the galactic background measured by PAMELA and FERMI sparked a significant interest in dark matter models which include resonant annihilation channels. In order for dark matter annihilation to produce the observed halo positron excess, a large thermally averaged dark matter annihilation cross section, $\langle \sigma v \rangle$ is needed. The order of magnitude estimates show that required $\langle \sigma v \rangle$ needs to be $O(100 - 1000)$ larger than the canonical $\langle \sigma v \rangle_0 \sim 10^{-9} GeV^{-2}$ required in the early universe by the estimates of dark matter relic abundance [2].

Dark matter annihilation through an s-channel resonance is a mechanism able to reconcile the conflict between the large cross section enhancements, or boost factors, needed to produce the positron excess in the halo and the small cross sections needed in the early universe to yield the correct relic abundance. The non-trivial velocity de-

[2]Estimates of dark matter relic abundance are in the context of the Standard Cosmological Model (ΛCDM), as measured by WMAP.

pendence of resonant cross section allows for the thermally averaged cross section in the early universe to be small, while enhancing the cross sections in the halo by orders of magnitude.

Long before the positron data was available, Griest and Seckel [36] noticed that resonant dark matter annihilation is a rich problem in the context of thermal relics. Typically, analytic calculations of relic abundance involve expansions of dark matter annihilations cross sections in partial waves. The expansions are usually presented as truncated polynomials in powers of velocity and are particularly useful for finding simple analytic solutions for relic abundance. Simple polynomial expansions of *resonant* annihilation cross sections however, cannot be used for calculations of dark matter relic abundance. The truncated series approximations are never accurate over the wide range of velocities needed, contradicting the standard estimate of a constant $\langle \sigma v \rangle_0 \sim 10^{-9} GeV^{-2}$. Analytic solutions are difficult for the same reason. Consequently, the effects of dark matter annihilation through a resonance could possibly have drastic effects on the magnitude of dark matter abundance in the present universe.

Resonant dark matter affects two very distinct areas of dark matter physics. One area concerns the dark matter relic abundance calculation and the early universe resonant annihilation processes. The other area concerns signals of dark matter annihilation today, in our own galactic halo. Simultaneously requiring fixed relic densities and accepting the possible signals of dark matter in the galactic halo creates a highly constrained problem on a multi-dimensional parameter space, with additional difficulties regarding multiple scales involved. We confront the problem of resonant dark matter annihilation by first analyzing relic abundance and halo annihilation separately. Separating the analysis this way allows for more controllable treatment of simultaneous relic abundance and halo annihilation constraints.

Most of the past work on resonant dark matter annihilation has been largely numerical and limited to a discussion of only a part of the resonant annihilation parameter set. In this work, we derive constraints on resonant dark matter annihilation parameters from relic abundance and the indirect detection experiments. We take into account the full set of resonant annihilation parameters and analyze it over a wide range of the multidimensional parameter space. We develop a number of novel analytic constraints, as well as perform an extensive numerical analysis of the multidimensional resonant dark matter annihilation parameter space.

Much of our work in dark matter is devoted to design and implementation of a comprehensive numerical package for particle dark matter physics called MadDM [37]. Our multi-purpose code is built on top of the existing MadGraph [38] architecture which provides the framework for calculating Feynman diagrams and the corresponding scattering amplitudes. At the present stage, given a model of dark matter, MadDM is able to automatically select dark matter candidates, generate all relevant annihilation processes and calculate the resulting relic abundance. Future versions of the code will include the capability to calculate cosmic ray fluxes relevant for indirect detection experiments and dark matter-nucleon scattering rates used in direct detection experiments. In addition, recently developed packages designed to include next-to-leading-order (NLO) Feynman diagrams in MadGraph could be used in MadDM as well. Ability to include NLO diagrams, and thus loop induced processes, will give MadDM a significant edge over all other publicly available dark matter codes.

The MadDM project continues to develop beyond the scope and timeline of this dissertation. With this in mind, only a portion of the MadDM code relevant for the work in the thesis is included in the Appendix.

The thesis is organized in four distinct units:

- In Chapter 2 we discuss a general form of the resonant annihilation cross section used for relic abundance calculations as well as the non-relativistic approximations appropriate for the analysis of dark matter annihilation in the galactic halo. Using the optical theorem, we derive the total resonant annihilation cross section which does not explicitly depend on the number or type of final state particles. Our form of the cross section allows for any general dependence on the spins of initial and intermediate states. In Section 2.3 we develop a non-relativistic approximation of the resonant annihilation cross section in the galactic halo as well as define the thermally averaged annihilation cross section $\langle \sigma v \rangle$.

- Chapter 3 contains a detailed discussion of our model independent relic abundance calculation and the limits on resonant dark matter annihilation from relic abundance. We present the technology needed to perform relic abundance calculations and explicitly list the assumptions made during its derivation. Section 3.2 deals with the effects of resonance poles on the temperature dependence of thermally averaged cross sections and consequently on relic abundance.

- In Chapter 4 we develop new analytic expressions describing the relationship between the dark matter mass, resonance mass, resonance width and couplings, as required by correct relic abundance. Our analytic relations give useful bounds for a wide spectrum of dark matter models which involve resonant s-channel annihilation. We make no assumptions about the location of the resonant pole relative to the dark matter production threshold nor the number or type of additional annihilation channels. The relations are robust enough to account for additional assumptions about the relevant parameters and additional channels specific models may require.

- In Chapter 5 we consider the requirements on cross section enhancements in order to explain the PAMELA and FERMI data. We first find model-independent upper limits on rates of dark matter annihilation in galactic halos. The Born level cross section generally fails to produce the desired enhancements. We show that exotic threshold enhancements akin to "Sommerfeld factors" [39, 40] are also innapropriate. Unitarity shows the Sommerfeld factors cannot produce large changes in cross sections, and serves to identify where those approximations break down. The most efficient annihilation mechanism involves perturbatively small decay widths that have largely been ignored. Widths that are very small compared to TeV mass scales, but large compared to the energy spread in the galactic halo suffice to cause large enhancements in the velocity averaged cross sections. Bound state formation in weakly coupled theories produces small effects due to wave function normalizations.

- In Chapter 6 we consider both the relic abundance constraint and the large cross section enhancements to obtain new limits on dark matter masses and couplings. Our results show that a significant degree of fine tuning is required in order to account for both the large enhancements and relic abundance. We find that previous attempts to fully analyze resonant dark matter annihilation in the galactic halo are flawed and concern only a subset of relevant parameters. Using only the width and the mass of the resonance in order to motivate large cross section enhancements, or boost factors, in the galactic halo never guarantees that the enhancements will actually be achieved. To correct this, we revisit the calculation including the complete parameter set. Previously overlooked limits on dark matter masses and couplings appear as a result.

- Appendix A.1 contains a detailed derivation of the Boltzmann equation commonly found in dark matter literature. We identify the approximations made during the derivation and explicitly list all the associated assumptions. Appendix A.2 contains a description and samples of the MadDM code used in this thesis.

Chapter 2

Resonant (Breit-Wigner) Annihilation Cross Section

Particle physics plays a major role in determining the properties of cosmological and astrophysical signatures of dark matter. In the current application of particle physics to Big Bang cosmology, relic abundance of thermal dark matter is largely determined by the total annihilation rate of dark matter in the early universe. In addition, dark matter annihilation rate in the galactic halo can be used to predict charged particle fluxes relevant to indirect detection experiments. None of these calculations can proceed without the input about dark matter annihilation cross sections coming from particle physics.

There are many models of particle dark matter, leading to a wide range of cosmological and astrophysical dark matter signatures. Here, we are interested in a *class* of models in which dark matter can annihilate via an s-channel resonance. Before we can perform any calculations and derive any limits, we first must discuss general forms of the resonant annihilation cross section and the corresponding thermally averaged cross section. In considering resonant dark matter annihilation, we do not put any assumptions on the type or the number of final states and we take into account many possible combinations of the initial states and the intermediate resonance spins. For the purpose of relic abundance calculations we use a general form of the resonant annihilation cross section derived in Section 2.2 from the optical theorem. Dark matter annihilation

in the galactic halo is highly non-relativistic, allowing for the use of a more practical non-relativistic approximation of the Breit-Wigner cross section.

2.1 Thermally Averaged Cross Section

Calculations of astro-particle fluxes and relic abundance are typically expressed in terms of the thermally averaged cross section $\langle \sigma v \rangle$, making it one of the central quantities in dark matter particle physics. In general, the thermally averaged cross section $\langle \sigma v \rangle$ can be defined as [41]

$$\begin{aligned} \langle \sigma_{X\bar{X}\to y_1 \ldots y_n} |v| \rangle &\equiv \frac{1}{n_{EQ}^2} \int dPS_X dPS_{\bar{X}} \prod_{i=1}^{n} dPS_{y_i} (2\pi)^4 \\ &\times \delta^4 (p_X + p_{\bar{X}} - \sum_i^n p_i) |M_{X\bar{X}\to y_1 \ldots y_n}|^2 \\ &\times \exp(-E_X/T) \exp(-E_{\bar{X}}/T), \end{aligned} \tag{2.1}$$

where

$$n_{EQ} = \frac{g_i}{2\pi^2} \frac{m^3}{x} K_2(x), \tag{2.2}$$

is the equilibrium number density of the species $X, \bar{X}$ expressed in terms of the dimensionless variable $x \equiv m/T$, and m is the mass of $X, \bar{X}$. Here g_i is the number of internal degrees of freedom of dark matter, $\beta = \sqrt{1 - 4m^2/s}$ and K_n is the modified Bessel functions of the second kind.

In Eq. 2.1 dPS stands for the Lorentz invariant phase space element

$$dPS \equiv \frac{1}{(2\pi)^3} \frac{d^3 p}{2E}. \tag{2.3}$$

For the purpose of numerical calculations, it is often useful to rewrite Eq. 2.1 as a one dimensional integral [41]:

$$\langle \sigma v \rangle = \frac{1}{n_{EQ}^2} \frac{m}{64\pi^2 x} \int_{4m^2}^{\infty} 4E_X E_{\bar{X}}\, \sigma v\, g_i^2\, \beta\, \sqrt{s}\, K_1\left(\frac{x\sqrt{s}}{m}\right) ds, \tag{2.4}$$

where $E_{X,\bar{X}}$ is the energy of initial state particles and σ is the total annihilation cross section, and v is the relative velocity of the colliding particles.

The form of $\langle \sigma v \rangle$ in Eq. 2.4 is appropriate for relic abundance calculations which span a wide range of energies. Dark matter in the galactic halo is highly non-relativistic, moving at velocities of only $v_0 \sim 10^{-3}$ [1]. It is then appropriate to use non-relativistic approximation of the thermal distributions and $\langle \sigma v \rangle$ for the purpose of halo dark matter calculations [2].

2.2 General Form of the Resonant Annihilation Cross Section

Resonant cross sections are characterized by rapid energy dependence and multiple scales that require special analysis.

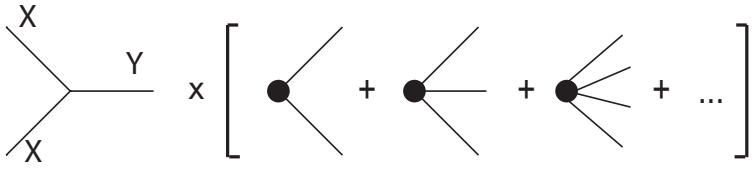

Figure 2.1: s-channel dark matter annihilation diagrams into all possible final states.

[1] Throughout this thesis, we use the term "velocity" to mean velocity rescaled by the speed of light c, in natural units: $c = \hbar = 1$.

[2] We postpone a more detailed discussion of the non-relativistic approximations of the thermally averaged annihilation cross section until Chapter 5.

Let $M_{X\bar{X}\to f}$ be the amplitude for XX to go to a final state f. The cross section σ goes like the amplitude-squared, summed over all final states (Fig.2.1), and integrated over final state phase space dPS:

$$d\sigma \sim \frac{1}{flux}\sum_f |M_{X\bar{X}\to f}|^2\, dPS.$$

The total cross section into all possible final states is given by the optical theorem:

$$\sigma_{tot} = -\frac{1}{2kE_{CM}} Im(M(s,t=0)).$$

Here k is the momentum of either particle in the center of mass frame, and M is the elastic scattering amplitude. For a given total center of mass energy E_{CM} and its square s, the forward propagators of intermediate states Y go like $(s-m_Y^2+im_Y\Gamma)^{-1}$, where Γ is the total width. Let $g^2_{XXY}t_{jj'}$ be the component of the elastic amplitude containing the couplings of the initial/final states of spin j to an s-channel particle of spin j'. Then the optical theorem predicts the total cross section σ_{tot} to be

$$\begin{aligned}\sigma_{tot}(s) &= -\frac{1}{2kE_{CM}} Im\left(\frac{g^2_{XXY}t_{jj'}}{s-m_Y^2+im_Y\Gamma_Y}\right) \\ &= \frac{b_f g^2_{XXY}}{2kE_{CM}}\frac{m_Y\Gamma_Y t_{jj'}}{(s-m_Y^2)^2+m_Y^2\Gamma_Y^2}. \end{aligned} \tag{2.5}$$

Here we included the branching ratio

$$b_f \equiv 1 - B_i, \tag{2.6}$$

where B_i is the branching ratio for the elastic channel to ensure that we account only for the events which change the number of dark matter particles [3]. We choose to leave b_f as a free parameter. Note that in many models, b_f and g_{XXY} can be combined since $B_i \equiv B_i(g_{XXY})$. Furthermore, in many models, B_i is small and slowly varying function of dark matter velocity allowing us to extract b_f as an overall constant. The symbol Γ_Y represents the total width of Y to all final states, which allows us to describe numerous models with a single parameter.

In standard convention for amplitudes, the Feynman rules contain in/out state polarization and vertex factors compiled into the symbol $t_{jj'}$. For heavy dark matter an-

Initial State	Intermediate State	$t_{jj'}$
SS	S'	$m_X^2/2$
SS	V	$4\vec{k}\|^2$
$\overline{f}f$	S	$m_X^2/4$
$\overline{f}f$	V	$2(3m_X^2+2\vec{k}\|^2)$
$\overline{f}f$	$\tilde{\mathrm{V}}$	$2(m_X^2+2\vec{k}\|^2)$
$\overline{f}f$	$\tilde{\mathrm{S}}$	$2(m_X^2+\vec{k}\|^2)$

Table 2.1: Value of the $t_{jj'}$ factor for some commonly found combinations of initial states and intermediate states. "S" stands for scalar, "f" for fermion, "V" for vector, "$\tilde{\mathrm{S}}$" for pseudo-scalar and "$\tilde{\mathrm{V}}$" for a pseudo-vector.

nihilation, we can extract the mass (m_X) dependence of these factors for analysis. We define

$$t_{jj'} = 4m_X^2 \frac{w_{jj'}}{(2j+1)^2} = 4m_X^2 C_{jj'}, \tag{2.7}$$

whereby $C_{jj'}$ is typically a number of order unity. Scaling like m_X^2 is expected from dimensional analysis, and inevitable when the initial state is dominated by the mass as the largest scale. We emphasize that $C_{jj'}$ is a definition that allows for any model while

[3] From here on, we will take symbols σ and σ_{tot} to mean annihilation cross section into all channels *but* the elastic channel.

postponing spin-sums and vertex factors until a model is chosen. For example, the annihilation of unpolarized Dirac Fermions via a γ^μ vertex produces $C_{1/21} = 3/2$. The coupling and spin factors then appear in the combination $4\pi a_{XXY} C_{jj'}$, where $\alpha_{XYY} = g^2_{XXY}/(4\pi)$. A list of different values of $t_{jj'}$ depending on different spin combinations are listed in Table 2.1

2.3 Non-Relativistic Form of the Resonant Annihilation Cross Section

Since they are gravitationally bound, relic particles trapped in galactic halos will be non-relativistic, with velocities $v \sim 10^{-3}$. There are several distinctly different non-relativistic resonant formulas. Most non-relativistic cross sections σ_{res} can be cast into the form

$$\sigma_{res} = \frac{4\pi v^N}{k^2} \frac{(\Gamma/2)^2 B_i B_f}{(E - E_{res})^2 + (\Gamma/2)^2} = \frac{4\pi}{k^2} BW(\Gamma, E_{res}). \tag{2.8}$$

Here B_i and B_f are the branching fractions to the initial and final state, and k is the momentum of an initial state particle in the center of mass frame. Different values of the parameter $N = 0, 1$ distinguish two classic limits:

Phase Space Limited Case, $N = 0$: It is common for $2 \to 2$ non-relativistic physics to be quasi-elastic. In particular, the *final* state phase space may be severely limited by the *initial* state velocity v. Ignoring spin and matrix elements, the Lorentz-invariant

phase space integral dPS for two particles of momentum p_f, p'_f and mass m_f: is

$$dPS = \int \frac{d^3p_f}{2p_f^0}\frac{d^3p'_f}{2p_f'^0}\delta^4(Q - p_f - p'_f)$$
$$= 2\pi\sqrt{1-4m_f^2/Q^2} = 2\pi v_f. \tag{2.9}$$

Here v_f is the final state velocity of either particle. When initial and final state masses are comparable, and the 2-body states dominate, the total width $\Gamma \sim \kappa v_f \sim \kappa v$, where κ absorbs coupling constants and matrix elements. Incorporating the explicit velocity dependence with an s-channel propagator leads to Eq. 2.8 with $N = 0$. Note that the peak of the cross section scales like $1/(m^2v^2)$, making this case potentially capable of saturating elastic unitarity bounds.

Relativistic Phase Space Case, $N = 1$: Anihillation may also proceed to final states which are ultra-relativistic. Then the square root in Eq. 2.9 approaches 1, and the partial width $\Gamma_f \sim$ *constant* in this limit. Any other kinematic situation where Q^2/m_f^2 goes to a finite constant as $v \to 0$ will produce the same outcome. This includes the "exoergic" resonances long known in low-energy nuclear physics, and associated with the "$1/v$ law" of low energy cross sections. These cross sections do not increase as fast as unitarity would allow as $v \to 0$.

The difference between $1/v$ and $1/v^2$ velocity dependence is dramatic. Yet it is only part of the story, because resonances may produce large cross sections either way. For example, neutron absorption cross sections on Gadolinium-157 exceeding *one hundred million barns* have been observed. [42]. This comes in the seemingly "mild" $1/v$ case not impinging on a unitarity limit. The experimental stunt simply exploits neutrons with grossly small velocities of order 3 meters per second. In much the same way, galactic halo velocities of order 10^{-3} are grossly small on the scale of particle physics.

The combination of low speed halo kinematics and very ordinary widths produces surprisingly large enhancements.

Chapter 3

Relic Abundance of Dark Matter

Models of particle dark matter can be divided into two distinct groups:

Thermal dark matter scenario assumes that in the early universe the number density of dark matter was in thermal equilibrium. As the universe expanded, the annihilation rate of dark matter was eventually surpassed by the expansion rate of the universe making it difficult for dark matter particles to continue to annihilate. Consequently, the number density of dark matter particles reached a constant asymptotic value, and thus led to a presence of dark matter in the current universe.

Non-thermal dark matter scenario assumes that the abundance of dark matter in the current universe was produced by a mechanism other than the thermal evolution of number density. For instance, axion dark matter could be produced during the QCD phase transition in the early universe, without much regard for the thermal evolution of cold relics. In this chapter, we will consider only resonant annihilation models of thermal dark matter.

Cosmological data offers a way to determine the relic abundance of dark matter in the present universe. Big bang cosmology predicts the existence of the cosmic microwave background (CMB) as a result of the recombination epoch. The CMB was first observer long ago by Penzias and Wilson [43, 44], who estimated the temperature

of the background radiation to be $\approx 3K$. Since then, the Cosmic Background Explorer (COBE) [45] and later the Wilkinson Microwave Anisotropy Probe (WMAP) [4] measured anisotropies in the CMB which allowed for extraction of cosmological parameters *given* a cosmological model.

One of the parameters which can be extracted from the CMB data is the relic abundance of dark matter. It is common to express dark matter relic abundance through a parameter

$$\Omega_\chi h^2 = \rho_\chi / \rho_c,$$

where ρ_χ is the mass density of dark matter and ρ_c is the critical density

$$\rho_c = 1.29 \times 10^{-29} g/cm^3 \, h^2. \tag{3.1}$$

In the last eqution h is the reduced Hubble parameter. In the context of the Standard Cosmological Model, WMAP estimates dark matter relic abundance in the current universe to be

$$\Omega_\chi h^2 \approx 0.1.$$

Viable particle physics models of thermal dark matter should naturally be able to accommodate the WMAP constraint on relic abundance.

3.1 Relic Abundance Calculation

In order to constrain particle models of dark matter using the WMAP results, we first need a way to calculate dark matter relic abundance in the present universe given a particle physics model. Statistical mechanics offers necessary tools. The Boltzmann equation of statistical mechanics relates time evolution of macroscopic phase space

distributions of dilute gasses with microscopic interaction rates between the gas and its environment. A cosmological version of the Boltzmann equation should also take into account the effects of the expanding universe. From the equation for phase space distributions, it is possible to obtain a rate equation for number densities and thus calculate the relic density of dark matter in the present universe. In the next section, we discuss a form of number density rate equation commonly found in dark matter literature. A more detailed derivation is given in the Appendix.

3.1.1 Boltzmann Equation

Dark matter relic abundance is calculated by solving a rate equation which relates the number density of dark matter with its annihilation rate and the expansion rate of the universe. Here we outline a procedure used to motivate such an equation [1].

In statistical mechanics, the statement of conservation of phase space volume is expressed by the Boltzmann equation:

$$\frac{df}{dt} = \left(\frac{\partial}{\partial t} + \frac{\partial \vec{x}}{\partial t}\frac{\partial}{\partial \vec{x}} + \frac{\partial \vec{p}}{\partial t}\frac{\partial}{\partial \vec{p}} \right) f = \frac{\partial f}{\partial t}_{col}, \tag{3.2}$$

where

$$f \equiv f(\vec{x}, \vec{p}, t), \tag{3.3}$$

is a phase space distribution and $\frac{\partial f}{\partial t}_{col}$ is a collision term. For a non interacting system $\frac{\partial f}{\partial t}_{col} = 0$. Defining the number density for a spatially isotropic distribution f to be

$$n \equiv \int d^3 p f(\vec{p}, t), \tag{3.4}$$

[1] Throughout this thesis, and for consistency with the rest of dark mater literature, we will refer to the number density rate equation as the Boltzmann equation.

leads to an equation for number density and thus relic abundance. The standard form of the number density rate equation found in many cosmology textbooks [41] makes the following assumptions:

1. There is only one species of dark matter.
2. The phase space distribution of the initial state particles in uncorrelated.
3. The dynamics is even under time reversal.
4. The metric is of a Robertson-Walker form.
5. The universe is expanding adiabatically.
6. All final state species are in thermal equilibrium.
7. The only species modeled to go out of equilibrium is the dark matter species.
8. There is no particle-antiparticle number asymmetry.
9. Effects of spin degeneracies are neglible.

The above assumptions reduce the collision term into a form

$$\frac{\partial n}{\partial t}_{col} = -\langle \sigma v \rangle (n^2 - n_{EQ}^2), \tag{3.5}$$

where n_{EQ} is the equilibrium distribution of the dark matter particle species. Taking into account the assumptions about the expanding universe, in terms of number density, Eq. 3.2 takes the form [41]:

$$\frac{dn}{dt} + 3Hn = -\langle \sigma v \rangle (n^2 - n_{EQ}^2), \tag{3.6}$$

where H is the Hubble parameter. For the purpose of both numerical and analytical calculations, the left side of Eq. 3.6 is somewhat cumbersome. It is often useful to redefine the Boltzmann equation in a more "calculation friendly" form. Defining $Y \equiv n/s$, where s is the entropy density defined below, and replacing time with $x = m/T$ produces the standard form of the cosmological Boltzmann equation from Ref. [41]:

$$\frac{dY}{dx} = -\frac{xs(x)\langle\sigma v\rangle}{H(m)}(Y^2 - Y_{EQ}^2). \tag{3.7}$$

Here

$$Y \equiv \frac{n}{s}; \qquad Y_{EQ} = \frac{45}{4\sqrt{2}\pi^{7/2}}\frac{g_i}{g_*}x^{3/2}e^{-x}. \tag{3.8}$$

This particular form of Y_{EQ} is valid for $x \geq 3$, the region of x relevant for relic density calculations. In Eq. 3.8 $s(x)$ is the entropy density defined as

$$s(x) = \frac{2\pi^2 g_{*S}}{45}\left(\frac{m}{x}\right)^3, \tag{3.9}$$

where g_{*S} is the number of relativistic degrees of freedom that contribute to the entropy density defined as

$$g_{*S} = \sum_{i=bosons} g_i\left(\frac{T_i}{T}\right)^3 + \frac{7}{8}\sum_{i=fermions} g_i\left(\frac{T_i}{T}\right)^3, \tag{3.10}$$

and $H(m)$ is the hubble parameter

$$H(m) = \sqrt{\frac{4\pi^3}{45}}\frac{\sqrt{g_*}\,m^2}{m_{pl}\,x^2}. \tag{3.11}$$

In Eq. 3.11 $m_{pl} = 1.22 \times 10^{19} GeV$ is the Planck mass and g_* is defined as

$$g_* = \sum_{i=bosons} g_i \left(\frac{T_i}{T}\right)^4 + \frac{7}{8} \sum_{i=fermions} g_i \left(\frac{T_i}{T}\right)^4 . \tag{3.12}$$

Note that the difference between g_* and g_{*S} is negligible for $T \geq 10^{-4} GeV$.

At very early times ($x \sim O(1)$), $Y_{EQ} \approx Y$, making the contributions of small x regions to $Y(\infty)$ miniscule. To a very good approximation, the asymptotic solution to the Boltzmann equation is then

$$Y_\infty = \left(\int_{x_d}^{\infty} dx \frac{x s(x) \langle \sigma v \rangle}{H(m)} \right)^{-1}, \tag{3.13}$$

where we define the decoupling time x_d as the time where $|Y(x_d) - Y_{EQ}(x_d)| = Y_{EQ}(x_d)$. It is also common to refer to x_d as the *freeze-out* time for cases where σ is a slowly varying function of energy.

In terms of the asymptotic solution Y_∞ the relic abundance parameter can be written as

$$\Omega_{DM} h^2 \equiv \frac{\rho_{DM}}{\rho_{crit}} = \frac{m Y_\infty s_0}{\rho_{crit}}, \tag{3.14}$$

where s_0 is the entropy density in the present universe.

The approximate solution of Eq. 3.14 can be further simplified for cases where the annihilation cross section is a slowly varying function of energy. In this case, the thermally averaged cross section $\langle \sigma v \rangle$ can be factored out of the integral, while the rest of the integrand integrates out trivially giving a closed form solution for relic density of dark matter. Using the WMAP estimate of $\Omega h^2 \approx 0.1$ in Eq. 3.14 then yields an

estimate for a dark matter thermally averaged annihilation cross section

$$\langle \sigma v \rangle = 3 \times 10^{-26} cm^3/s \approx 10^{-9} GeV^{-2}. \tag{3.15}$$

The numerical value of Eq. 3.15 coincides with dark matter of electro-weak scale mass and couplings, prompting a label "the WIMP[2] miracle." At this point, we stress that Eq. 3.15 is an estimate of the dark matter annihilation cross section with the traditional assumption of $\langle \sigma v \rangle \neq \langle \sigma v \rangle(x)$. A part of our goal in this thesis is to break this tradition and explore more challenging and interesting alternatives. As we will show in the following sections, resonant dark matter annihilation strongly contradicts the estimates of Eq. 3.15.

3.2 Temperature Dependence of Resonant Thermally Averaged Cross Section and its Effects on Relic Abundance

Resonant annihilation of dark matter can have dramatic effects on the thermal evolution of its number density and consequently on relic abundance. In many ways, resonant dark matter annihilation contradicts the standard assumptions of Born-level cross sections.

The thermally averaged cross section $\langle \sigma v \rangle$ can be seen as a measure of the overlap of the annihilation cross section σ and the distribution of dark matter speed $\Phi(v)$. For the purpose of illustration, we can thus rewrite Eq. 2.1 as

[2]Weakly Interacting Massive Particle (WIMP)

$$\langle \sigma v \rangle = \int dv \, \sigma \, v \, \Phi(v,x). \tag{3.16}$$

Born-level estimates of dark matter annihilation cross sections usually assume partial wave expansions of the form

$$\sigma v = a + b\, v^2 + \ldots , \tag{3.17}$$

resulting in

$$\langle \sigma v \rangle = a' + b'/x + \ldots \tag{3.18}$$

It is important to point out that expansion in Eq. 3.18 commonly used to evaluate relic densities inevitably fails if the cross section is of the resonant form in Eq. 2.5 or similar. To justify, consider a series approximation of $\langle \sigma v \rangle$, for a pole below threshold, obtained by integration by parts:

$$\begin{aligned} \langle \sigma v \rangle \sim \frac{2}{x} BW(E=0,\Gamma_Y,m_Y) + \frac{4}{x^2} BW'(E=0,\Gamma_Y,m_Y) \\ + \frac{8}{x^3} BW''(E=0,\Gamma_Y,m_Y) + \ldots , \end{aligned} \tag{3.19}$$

where E is the kinetic energy of dark matter particles in the center of mass frame and BW is the dimensionless Breit-Wigner form-factor

$$BW \equiv \frac{m_Y \Gamma_Y t_{jj'}}{(s-m_Y^2)^2 + m_Y^2 \Gamma_Y^2}. \tag{3.20}$$

Looking at the derivatives of BW with respect to E shows that this expansion is valid only where $\Gamma_Y/m_X, (2m_X - m_Y)/m_X \gtrsim 1/x$. Take for example $\Gamma_Y/m_X, (2m_X - m_Y)/m_X = 10^{-2}$. The approximation fails for $x \leq 100$, a region crucial for the relic abundance calculation. In conclusion, if the width of the Breit-Wigner distribution is less than the

width of the velocity distribution, the magnitudes of higher derivatives cannot be guaranteed to be small, making any expansion in powers of x unreliable over a wide range of integration.

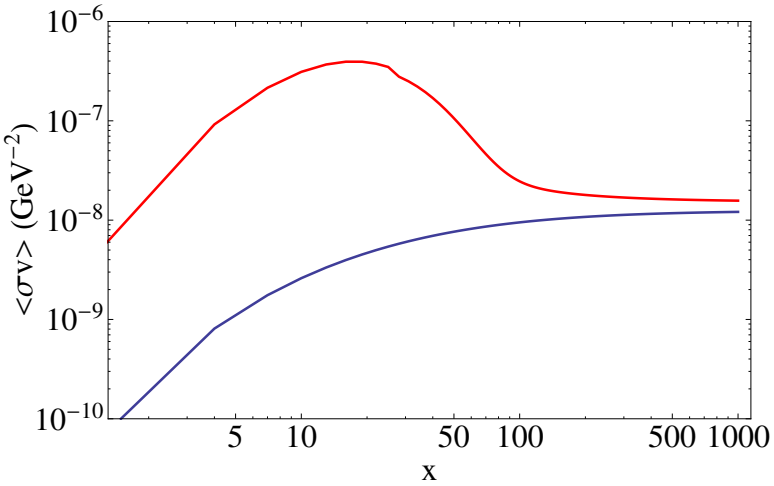

Figure 3.1: Thermally averaged cross section for a pole below threshold (blue line on the bottom) and above threshold (red line on the top). Parameters used for the purpose of the graphics are $m_X = 300GeV$, $g_{XXY} = 0.1$, $\Gamma_Y = 3GeV$. The resonance below threshold lies $30GeV$ below the threshold $2m_X$, while the above threshold case is just $30GeV$ above the threshold. Notice that in both cases $\langle\sigma v\rangle \approx a + b/x + ...$ is not a good approximation.

The effects of resonances on $\langle\sigma v\rangle$ can be dramatic. Consider a case in which only the s-wave component is relevant. Then the Born level estimate gives $\langle\sigma v\rangle \sim const$. An s-wave resonance is almost never this simple. Fig. 3.1 illustrates the result for a resonance below and above threshold. In the case of a resonance below threshold, $\langle\sigma v\rangle$ is an increasing function of x, which can have drastic effects on the resulting relic abundance of dark matter. A resonance above threshold can cause $\langle\sigma v\rangle$ to increase for a period of time and then decrease to a constant level. This is to be expected because the overlap between the cross section σ and the velocity distribution $\Phi(v,x)$ will be the greatest when $m_Y \approx T$.

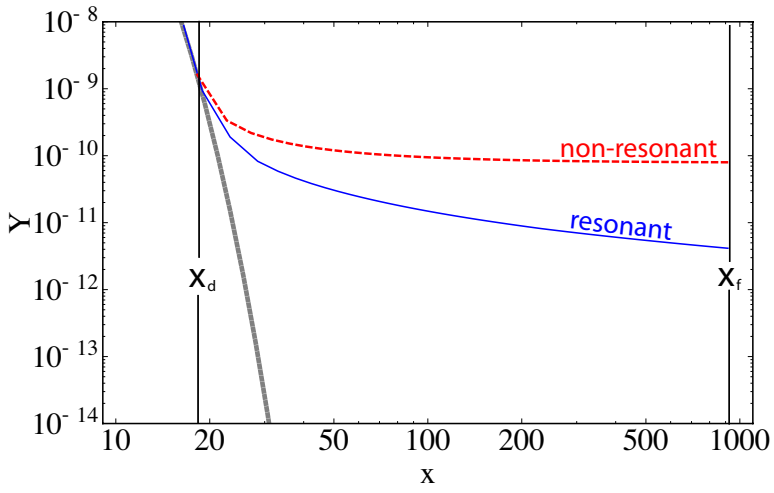

Figure 3.2: Thermal evolution of dark matter number density. Red dashed line represents the thermal evolution for a case of a constant $\langle \sigma v \rangle$. Thermal evolution for resonant dark matter annihilation is the blue line. For the purpose of the graphic, the resonance was tuned to a value slightly below $2m_X$, and a width of $O(1)GeV$ was assumed. Resonant and non-resonant cases were arranged so that they decouple from equilibrium at roughly the same time for better presentation. The thick gray line is the equilibrium distribution

In addition, identifying the temperature at which the number density of dark matter decouples from the equilibrium distribution as the freeze-out temperature is not appropriate in the case of resonant dark matter annihilation. Consider again a resonant pole below threshold. Since $\langle \sigma v \rangle$ increases with x, the expansion rate of the universe takes longer to "catch up" with the annihilation rate of dark matter. As a result, dark matter could in principle annihilate long after its number density decouples from the equilibrium distribution. Fig. 3.2 illustrates this point. Thermal evolution of dark matter number density decouples from the equilibrium distribution at roughly $x_d \approx O(10)$ in both the resonant and non-resonant case. However, in the non-resonant case the number density freezes out at x_d, while the number density for a resonant case continues to decrease until $x_f \approx 1000$.

Chapter 4

Analytic Mass-Width Relations

Finding an analytic solution to the Boltzmann equation using the cross section in Eq. 2.5 is non-trivial. In this section we show how to find simple relations between all the parameters of Eq. 2.5 *given* correct relic abundance. The procedure involves a combination of numerical and analytical calculations we develop here.

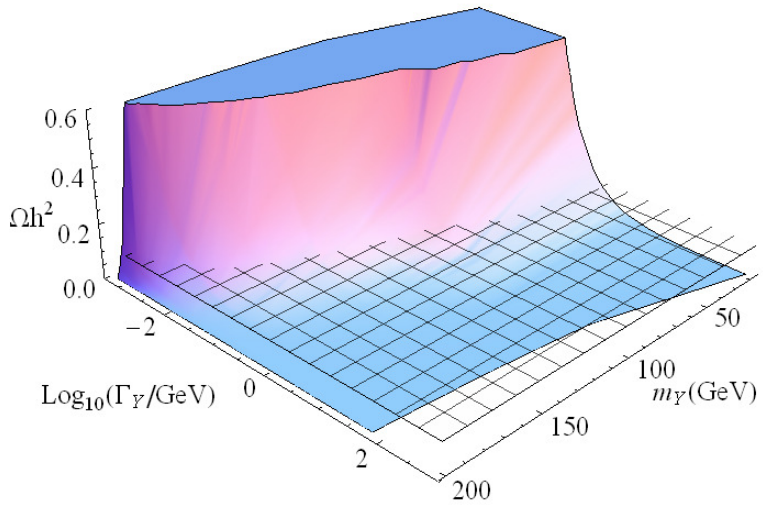

Figure 4.1: Intersection of the mesh plane representing $\Omega h^2 = 0.1$ and the surface $\Omega h^2(\Gamma_Y, m_Y, m_*, \alpha_*)$ gives a unique curve $\Gamma(m_Y)$. $m_* = 100GeV$, $\alpha_* = 0.01$ for the purpose of the graphic. Contours of $\Omega h^2 = 0.1$ for a set of different dark matter masses are presented in Fig. 4.2

In our numerical work we first choose a particular dark matter mass $m_X = m_*$ and coupling α_*. We then compute thousands of relic densities covering the Γ_Y, m_Y plane. The condition $\Omega(\Gamma_Y, m_*, m_Y, \alpha_*)h^2 \to 0.1$ produces a unique curve Γ_Y versus m_Y, namely the function $\Gamma_Y = \Gamma_Y(m_Y; m_*, \alpha_*)$. An example is shown in Fig. 4.1. With the scaling relations in hand, the curves are extended to numerical predictions for the general functional dependence of $\Gamma = \Gamma(m_Y; m_X, \alpha_{XYY})$ consistent with $\Omega h^2 = 0.1$.

In the next section, using a combination of kinematics, limiting behavior of resonant cross sections and intuition we show how to compress the extensive multi-parameter numerical calculation into simple analytic approximations.

4.1 Mass-Width Relations: Pole Below Threshold ($m_Y < 2m_X$)

Finding an analytic solution for relic abundance in the case of resonant annihilation is difficult. Rapid energy dependence of the cross section as well as the presence of multiple scales complicates the problem beyond the analytic estimates of relic density using either constant or polynomial $\langle \sigma v \rangle$. In this section, we show that even though the problem cannot be solved analytically exactly, it is possible to derive very good analytic approximations which constrain the full resonant annihilation parameter set given a fixed relic abundance.

Fig. 4.2 shows the mass-width relation as a family of curves plotted for selected m_X. The trend is that the further the m_Y is from the threshold, the larger Γ_Y must be needed to keep relic densities constant, and vice versa. This is because the proximity to threshold (rather than the absolute size) of m_Y is the dominant effect. Poles closer to

the threshold make for larger cross sections, which need to be compensated by smaller width.

This quantitative understanding leads to useful analytic formulas relating parameters of resonant dark matter annihilation over a wide range of parameter space.

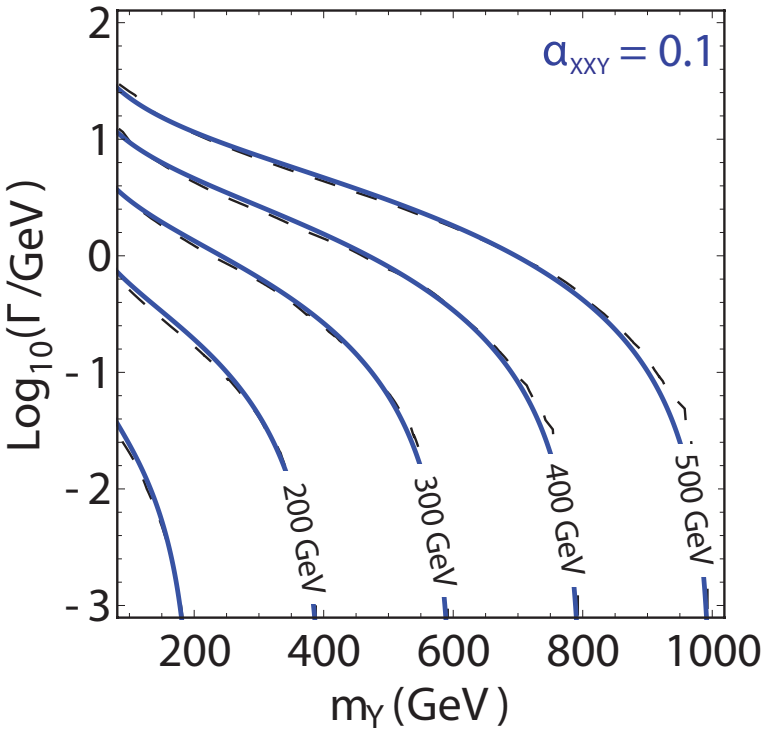

Figure 4.2: Relation of the s-channel width Γ_Y and mass m_Y *for a pole below threshold* consistent with cosmological relic density $\Omega h^2 = 0.1$. Dashed curves (black) are the numerical calculation. Solid curves (blue) are the analytic relation of Eq. 4.3. Each curve is evaluated with a fixed dark matter mass m_X =100-500 GeV in 100 GeV increments.

4.1.1 Analytic Representation

Observe in Fig. 4.2 that each dashed (black) curve moving to the right terminates in a region of $\Gamma_Y \to 0$. Near the threshold everything is determined by the degree of the zero of the function, $\Gamma_Y \sim (m_Y - 2m_X)^n$. The power $n = 2$ can be gotten analytically,

but was also fit directly with numerical work. Then we know $\Gamma_Y \sim (1 - m_Y/2m_X)^2$, times a known factor of m_X

In the opposite extreme of $m_Y << 2m_X$ the velocity averaged cross section $\langle\sigma v\rangle$ reduces to another simple analytic result:

$$\langle\sigma v\rangle(m_Y << 2m_X) \to \frac{\pi\alpha_{XXY}b_f C_{jj'}}{4m_X^4} m_Y\Gamma_Y. \tag{4.1}$$

Notice the dependence going like $m_Y\Gamma_Y$. Inverting the equation gives

$$\Gamma_Y \to \frac{4m_X^4}{\pi\alpha_{XXY}b_f C_{jj'}m_Y}\langle\sigma v\rangle. \tag{4.2}$$

The limit of small resonance mass $m_Y \to 0$ with $\Gamma_Y << 2m_X$ approaches the Born approximation, and for us is the unique case where the Born cross section is relevant. In the Born limit we know $\langle\sigma v\rangle \to 3\times 10^{-26} cm^3/s$, which fixes one overall scale. Then accounting for factors of m_X gives

$$\begin{aligned}\Gamma_Y \sim \frac{4m_X^3}{\pi C_{jj'}\alpha_{XXY}b_f}&(2.6\times 10^{-9} GeV^{-2}) \\ &\times\left(1-\frac{m_Y}{2m_X}\right)^2 \frac{m_X}{m_Y} g(m_Y/m_X).\end{aligned}$$

The dimensionless interpolating function $g(m_Y/m_X)$ remains. It must obey $g \to 1$ when $m_Y << 2m_X$, suggesting a polynomial expansion $g \sim 1 + \sum_k g_k (m_Y/m_X)^k$. Two terms suffice with $g_1 = 2$. Our analytic formula for the *pole below threshold mass-width*

relation is then

$$\begin{aligned}\Gamma_Y &= \frac{8}{\pi}\frac{1\,GeV}{C_{jj'}\alpha_{XXY}b_f}\left(\frac{m_X}{730\,GeV}\right)^3 \\ &\times \left(1+\frac{m_X}{2m_Y}\right)\left(1-\frac{m_Y}{2m_X}\right)^2, \\ &\quad for\ m_Y < 2m_X. \end{aligned} \tag{4.3}$$

The fit of the formula to the numerical work is extremely good. Fig. 4.2 shows a typical example[1]. We have already noted that Eq. 4.3 generalizes and replaces the traditional formula $\langle\sigma v\rangle = 3\times 10^{-26} cm^3/s$. The formula accounts for the fact that intermediate states of all particles coupling to dark matter are either absolutely stable or have a finite lifetime. To underscore the difference, compare the traditional counting rules, motivated on dimensional analysis, using annihilation cross sections of order 1-picobarn. Under the assumption $\langle\sigma v\rangle \sim \alpha_X^2/m_X^2 \sim O(1)pb$, a typical upper limit $\alpha_X^2 \lesssim 10^{-4}$ would imply $m_X \lesssim 200$ GeV. This well-known result needs a finely tuned mass-couping relation to make a Universe. Our formula contains far more information, and reveals the hidden assumption that $m_Y << m_X$ was implicitly assumed for the traditional formula to be consistent.

4.1.2 Replacement Rule for Adding Non-Resonant Channels

Many models of dark matter annihilation include more than one channel. No matter how many channels are involved, as long as the s-channel is a part of the model, the mass-width relation of Eq. 4.3 leads to a useful, more general bound.

For definiteness, suppose the addition of other processes *increases* the annihilation rate. Then the theory keeping Ωh^2 fixed will require smaller Γ_Y, all other things fixed.

[1] We have used the γ^μ vertex throughout this chapter for the purpose of the graphics

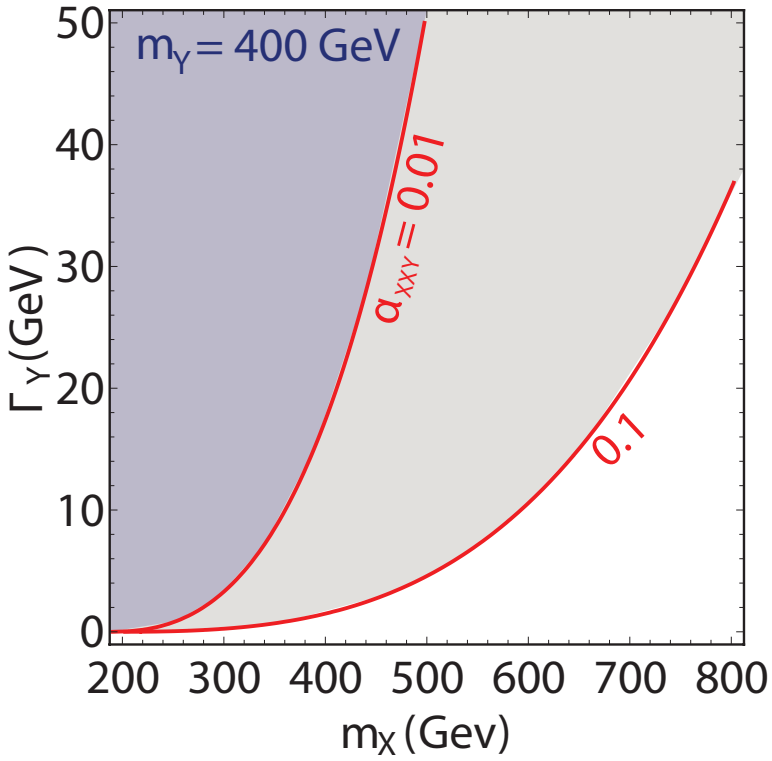

Figure 4.3: Upper limits on Γ_Y assuming s-channel annihilation (pole below threshold) plus other channels increasing the cross section. Shaded regions to the left and above the contours are not allowed. Curves show different couplings $\alpha_{XXY} b_f = g^2_{XXY}/4\pi$; $m_Y = 400 GeV$ is used for the purpose of the graphic. Larger m_Y pushes contours to the right.

That condition rules out all contours *to the right and above the contours* shown in Fig. 4.2 created by s-channel dominance. The *allowed region to the right and below* each line implies an inequality (Fig. 4.3) :

$$\Gamma_Y \leq \frac{8}{\pi}\left(\frac{1\,GeV}{C_{jj'}\alpha_{XXY} b_f}\right)\left(\frac{m_X}{730\,GeV}\right)^3 \times \left(1+\frac{m_X}{2m_Y}\right)\left(1-\frac{m_Y}{2m_X}\right)^2. \quad (4.4)$$

While cross sections often increase when channels are added, destructive interference occurs in some models. In that case the inequality reverses the sign.

To illustrate the use of Eq. 4.4, suppose a new vector boson (Z' perhaps) is discovered at the LHC [46–48]. Measuring the resonance observed in *any* channel will give its mass m_Y, and the *total* width Γ_Y. Applying Eq. 4.4 then gives the consistent m_X, $\alpha_{XXY} b_f$ parameter space regions consistent with relic abundance *without a need for an extensive numerical parameter space scan*. These *predicted* coupling relations are then compared to the information from production rate and branching ratio into particular channels seen in the experiment.

A new relation comes from a "replacement rule." Let the total velocity averaged cross section be expressed as

$$\langle \sigma v \rangle_{tot} = \langle \sigma v \rangle_s + \langle \sigma v \rangle_{other}.$$

Suppose $\langle \sigma v \rangle_{other}$ happens to be consistent with the traditional Born-style of approximation, by which

$$\langle \sigma v \rangle_{other} = \sum_i \alpha^i_{eff} / m_X^2,$$

where α^i_{eff} is an effective coupling to the i^{th} channel. (An example model in the context of heavy hidden sector dark matter can be found in Ref. [49].) Matching the extreme limits produces the replacement rule. If the s-channel pole is near the threshold, the mass width relation should approach Eq. 4.3. If the pole is far from threshold the resonant cross section approaches an effective Born-level cross section, and adds to it. That implies a boundary condition of $\langle \sigma v \rangle_s + \langle \sigma v \rangle_{other} \approx 10^{-9} GeV^{-2}$ at this endpoint.

Reviewing how that scale previously entered the analysis suggests a replacement rule:

$$2.6\times10^{-9}GeV^{-2}\rightarrow 2.6\times10^{-9}GeV^{-2}-\frac{\sum_i \alpha^i_{eff}}{m_X^2}. \tag{4.5}$$

The revised mass-v-width relation then becomes

$$\begin{aligned}\Gamma(m_Y) &= \frac{8}{\pi}\frac{1\,GeV}{C_{jj'}\alpha_{XXY}b_f}\left[1-\sum_i \alpha^i_{eff}\left(\frac{730\,GeV}{m_X}\right)^2\right] \\ &\quad\times(\frac{m_X}{730\,GeV})^3\left(1+\frac{m_X}{2m_Y}\right)\left(1-\frac{m_Y}{2m_X}\right)^2.\end{aligned} \tag{4.6}$$

Fig. 4.4 shows the replacement rule performs quite well. Not surprisingly, the difference relative to a pure *s*-channel annihilation model increases for smaller m_X. This is because the individual cross section contributions from other channels shown in Eq. 4.6 scale uniformly like $1/m_X^2$.

4.1.3 Calculable Widths Constrain the Masses

Up to here the width Γ_Y has been used as an independent parameter. We now go a step further and consider widths as quantities which can be calculated. When we say that "widths are calculable" it emphasizes the facts that (1) most theories are perturbatively coupled, and (2) most of the width will usually occur in a finite number of channels. Since we are developing a method for relating observables, we are not concerned with a model, and it suffices that widths exist as "trivial" once any particular model is defined. *Whatever the model*, combining the calculation of the width with the mass-width relation creates a new relation.

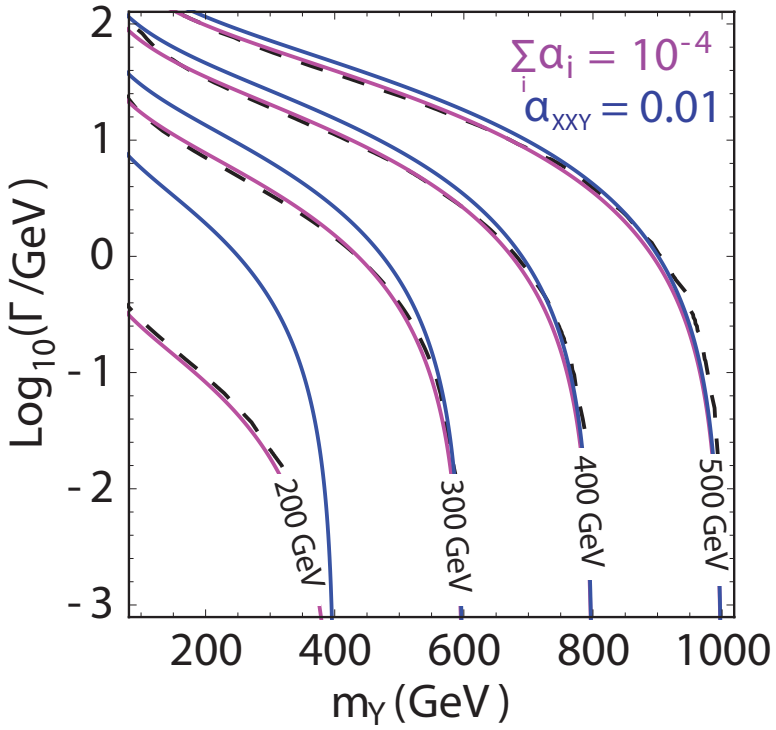

Figure 4.4: Generalization of the mass-width relation to include "Born-like" channels. Black dashed curves show numerical evaluation. Solid curves (magenta) are the revised fit of Eq. 4.6. Thick solid curves (blue) are the approximations of Eq. 4.3, consistent with the role as an upper bound. Different curves use different masses $m_X = 100 - 500GeV$, from left to right. Parameter $\alpha_{XXY} b_f = 10^{-2}$ and $\sum_i \alpha^i_{eff} = 10^{-4}$ for the purpose of the graphic.

The differential rate $d\Gamma$ of a general decay of a particle of mass m_Y is given by

$$d\Gamma \sim \frac{1}{2m_Y} |M|^2 dPS.$$

Symbol M is the amplitude. The final state phase space of two identical particles yield $\int dPS_2 \sim v_f$ where v_f is the velocity of either final state particle in the center of mass frame. In many cases the width is dominated by relativistic final states, $v_f \to 1$. It would be unusual, and a case of rather fine tuning, for all channels with phase space limitations $v_f << 1$ to dominate the total width.

Barring that event, by dimensional analysis, the width of a heavy particle with dimensionless coupling *always* depends on at least one overall power of its mass, which can be factored out:

$$\Gamma_Y \sim \alpha_\Gamma m_Y. \tag{4.7}$$

We make this an equality *by definition* allowing symbol α_Γ to absorb coupling constants, the number of important channels, and model details.

In general, α_Γ can still be a function of the mass m_Y, but this is a trivial effect which can be taken into account on a model by model basis. For example, $\Gamma_Y \sim m_Y^3$ occurs in many theories with a Higgs-type Yukawa coupling. We will then spare the reader separate sections and subsections for each dimensionful case, assuming it is agreed that symbol α_Γ stands for the width actually calculated in a particular model.

We continue by illustrating the method graphically for $\alpha_\Gamma \sim constant$. The formula for Γ_Y is an *increasing* function of m_Y. Meanwhile the s-channel mass-v-width requirements are all *decreasing* functions of m_Y (Fig. 4.2, Eq. 4.3, Eq. 4.6). Then the width-v-mass relation always crosses the s-channel mass-v-width relation at a definite point. Fig. 4.5 shows $\Gamma_Y = \alpha_\Gamma m_Y$ as red curves, whose intersections with the blue curves constrain the masses.

Inspection finds a useful fact. Rather weakly coupled theories ($\alpha_\Gamma \lesssim 10^{-4}$) only intersect the relic curves in the region where $m_Y \approx 2m_X$. In minimal supersymmetry, this result corresponds to the so called higgs "funnel" region of $m_0, m_{1/2}$ parameter space [50, 51]. However, our result is much more general and extends beyond the assumptions of SUSY.

The two couplings, α_Γ and α_{XXY} act in the same direction. Smaller α_Γ makes smaller widths that force the system into the threshold region to be viable. Smaller

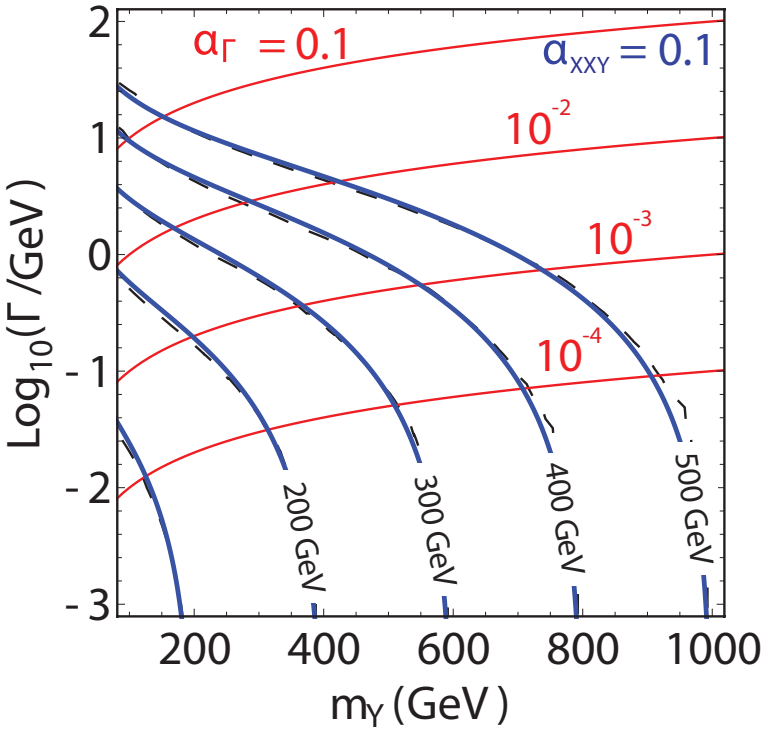

Figure 4.5: Combining the *below-threshold* width-v-mass m_Y relation of Fig. 4.2 with $\Gamma_Y = \alpha_\Gamma m_Y$ represented by solid thin curves (red). Intersections of the curves predict a non-linear relation between m_X and m_Y (text). Values of $\alpha_\Gamma = 10^{-1}$ (top curve) range to $\alpha_\Gamma = 10^{-4}$ (bottom curve) in factor of 10 increments.

α_{XYY} worsens the situation by pushing the contours of constant Ωh^2 up in the $\Gamma_Y - m_Y$ plane. The trend of both pushes masses into very near coincidence of $m_Y \sim 2m_X$, which we call a "finely-tuned threshold."

Except for bound state formation we have no reason to consider finely-tuned thresholds very plausible, but we include it for completeness. Bound states have been discussed in detail in Refs. [52, 53]. Some basic relations between bound state widths and masses are reviewed in Ref. [54]. Bound state relations are very specific and require separate treatment that is not our topic here.

Our mass-width relation allows for classification of models according to the degree of fine tuning. For example, Fig. 4.5 shows a theory with $\alpha_{XXY} b_f = 0.1$. The in-

tersections are not very demanding, and the theory is not finely tuned for $\alpha_\Gamma \geq 10^{-3}$. However the same theory using $\alpha_{XXY} b_f = 10^{-3}$ will require widths 100 times bigger for the same m_Y to keep Ωh^2 constant. At that point all contours are pushed up to such a degree we'd find the theory finely-tuned for all reasonable Γ_Y.

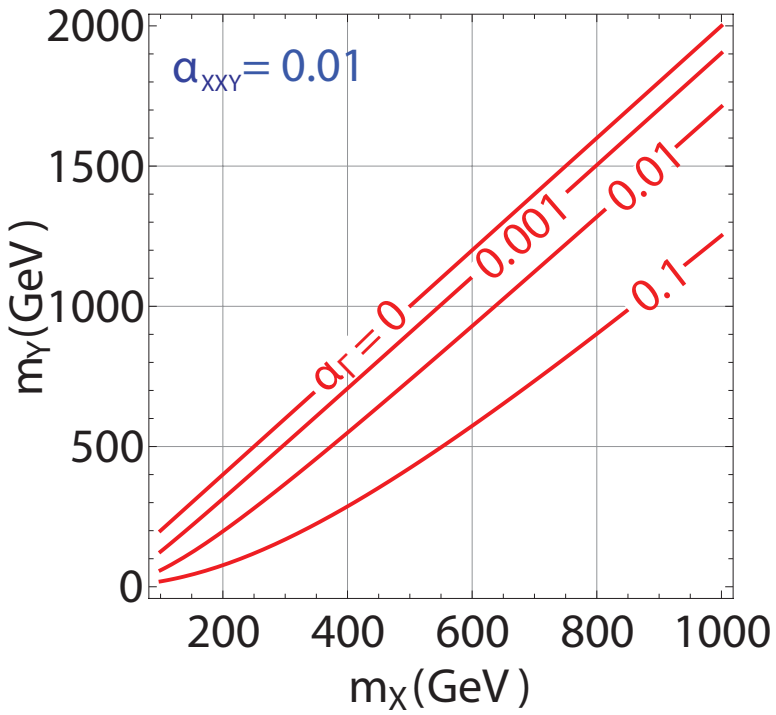

Figure 4.6: Mass of dark matter m_X versus the mass of the particle in the s-channel m_Y. Red lines represent $\alpha_\Gamma = 0.001, 0.01, 0.1$ from top to bottom. $\alpha_{XXY} = 0.01$ for the purpose of the graphic. Small widths (α_Γ small) require fine mass tuning, $m_Y \approx 2m_X$ to accommodate correct relic abundance.

4.1.4 Dark Matter and Pole Mass Relations

So far we have looked at an m_Y - Γ_Y relationship, given m_X. It is very interesting to consider the relation between m_Y and m_X given α_Γ. Fig. 4.6 shows the mass relationships for different values of α_Γ. Once again $\alpha_\Gamma \to 0$ forces the resonance into the finely tuned region of $m_Y \approx 2m_X$.

Solving Eq. 4.3 yields a cubic equation fixing $m_Y = m_Y(m_X, \alpha_{XXY} b_f, \alpha_\Gamma)$. The relationship is nearly linear for a wide range of m_X. Collect the couplings into a new symbol

$$\alpha_\kappa^2 = \frac{\alpha_{XXY}\alpha_\Gamma C_{jj'}}{10^{-4}}.$$

Note the symbol has been re-scaled in units of $\alpha_{XXY}/10^{-2}$, $\alpha_\Gamma/10^{-2}$ we find reasonable. The series expansion for large m_X is found to be

$$\begin{aligned} m_Y \approx 2m_X - 313GeV\,\alpha_\kappa + 40.2GeV\,\alpha_\kappa^2 (\frac{730GeV}{m_X}) \\ -5.87GeV\,\alpha_\kappa^3 (\frac{730GeV}{m_X})^2 + \cdots . \end{aligned} \tag{4.8}$$

Eq. 4.8 with only the first two terms kept is essentially exact for $\alpha_\kappa \lesssim 1, m_X \gtrsim 100$ GeV, while for $\alpha_\kappa \gtrsim 1$ a numerical evaluation is preferable.

Analyzing Fig. 4.6 and 4.7 we notice that the mass range of 100-500 GeV does not require extreme fine tuning for a reasonable range of perturbative couplings. On the other hand the regime of $m_X >> 100GeV$ seems to require a pole tuned very finely according to Eq. 4.8.

4.2 Mass-Width Relations: Pole Above Threshold ($m_Y > 2m_X$)

The relic abundance calculation for a pole above threshold is complicated by a saddle point in the integration of $\langle \sigma v \rangle$. To begin we again consider the extreme limits. For

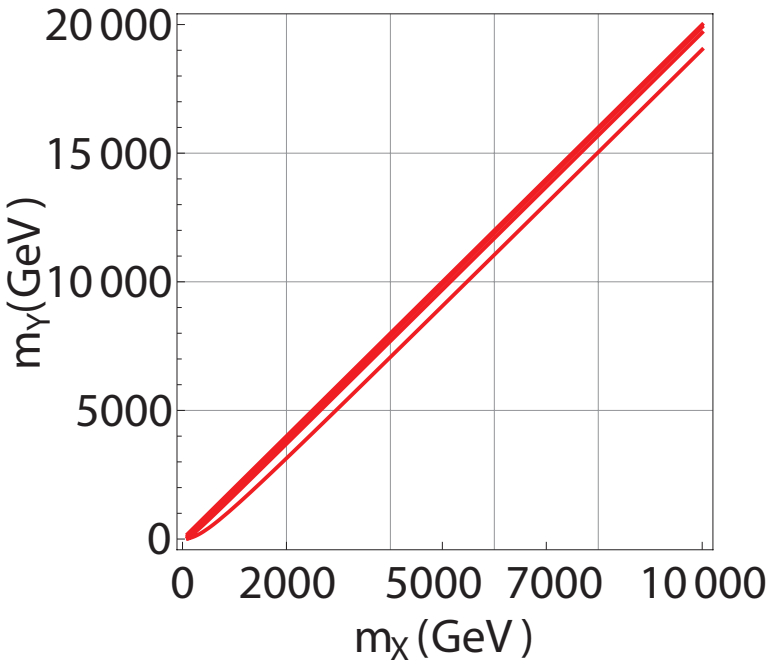

Figure 4.7: Same as Fig. 4.6 but for an extended range of m_X. Red lines represent $\alpha_\Gamma = 0.001, 0.01, 0.1$ from top to bottom. $\alpha_{XXY} = 0.01$ for the purpose of the graphic.

$m_Y >> 2m_X$ the velocity averaged cross section reduces to

$$\langle \sigma v \rangle (m_Y >> 2m_X) \rightarrow \frac{4\pi\alpha_{XXY} b_f C_{jj'}}{m_Y^3} \Gamma_Y. \tag{4.9}$$

By construction this limit reproduces the Born-level estimate, $\langle \sigma v \rangle \approx 10^{-9} GeV^{-2}$. Introduce a dimensionless function h to describe other limits, expressed by

$$\begin{aligned} \Gamma_Y \quad \sim \quad & \frac{m_Y^3}{4\pi\alpha_{XXY} C_{jj'}} (6.4 \times 10^{-9} GeV^{-2}) \\ & \times h(m_Y, m_X, A, \alpha_{XXY} b_f C_{jj'}). \end{aligned}$$

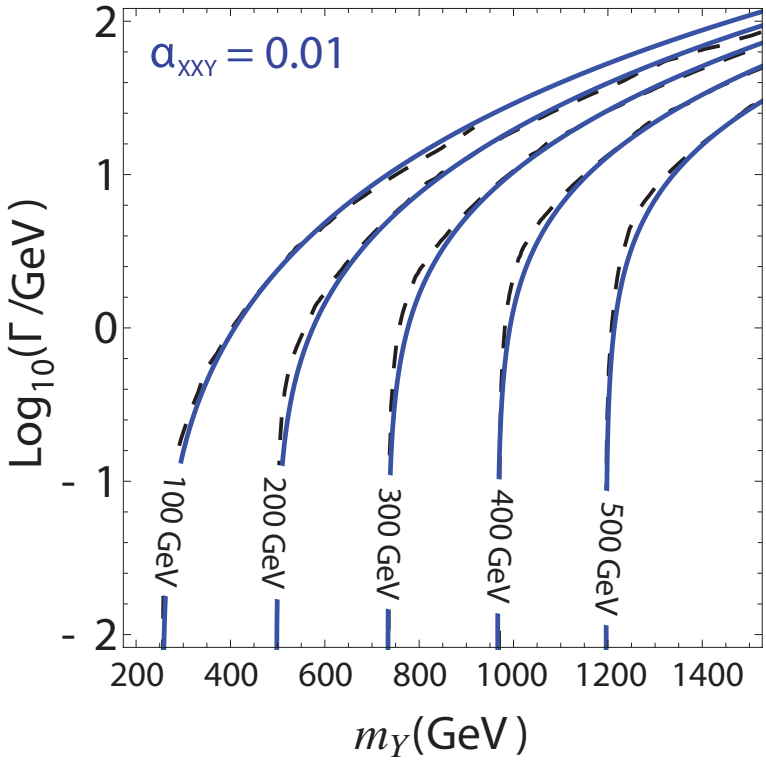

Figure 4.8: Relation of the s-channel width Γ_Y and pole mass m_Y *above threshold* consistent with cosmological relic density $\Omega h^2 = 0.1$. Dashed curves (black) are the numerical calculation. Solid curves (blue) are the analytic relation of Eq. 4.13. Each curve is evaluated with a fixed dark matter mass m_X =100-500 GeV in 100 GeV increments.

We have normalized $h \to 1$ for $m_Y >> 2m_X$ by absorbing the overall normalization into $6.4 \times 10^{-}9 GeV^{-2}$, suggesting the ansatz

$$h = 1 - \frac{\eta\, m_X}{m_Y}, \tag{4.10}$$

where η is the measure of the "offset" of m_Y from the threshold $2m_X$. Unlike the case of pole below threshold, the saddle point causes η to be a function of m_X and a relic scale parameter, which we call A.

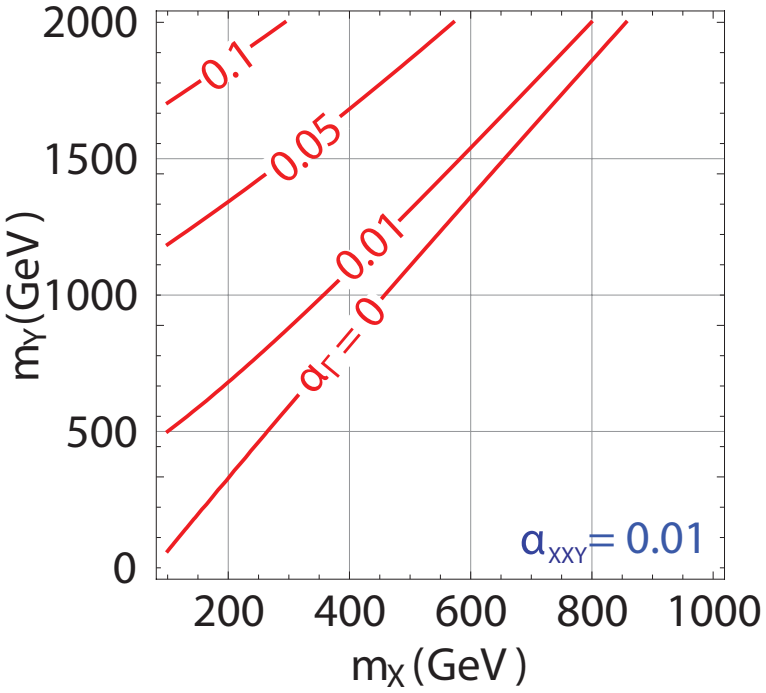

Figure 4.9: Mass of dark matter m_X vs. the mass of the s-channel particle m_Y for a pole above threshold, $m_Y > 2m_X$ Red lines represent $\alpha_\Gamma = 0, 0.01, 0.05, 0.1$ from top to bottom. $\alpha_{XXY} = 0.01$ for the purpose of the graphic. Small widths (α_Γ small) require very fine tuning of masses, $m_Y \approx \eta m_X$ to accommodate correct relic abundance.

The extreme of $\Gamma \to 0$ gives more information about the function h. The Breit-Wigner factor can be approximated as

$$\frac{\Gamma m_Y}{(s-m_Y^2)^2 + (m_Y\Gamma)^2} \to \pi\delta(s-m_Y^2). \tag{4.11}$$

The Boltzmann equation is then solved analytically in terms of error functions, predicting h and η in this limit:

$$\eta(m_X, \alpha_{XXY} b_f, C_{jj'}) \equiv 2\sqrt{1 + \frac{2}{x_d} erfc^{-1}\left(\frac{A m_X^2}{\alpha_{XXY} b_f C_{jj'}}\right)}, \tag{4.12}$$

where $A = 1.3 \times 10^{-11} GeV^{-2}$ gives a good fit for all reasonable m_Y and Γ_Y. The lower integration limit x_d is computed in a self consistent way and we find that the standard value of $x_d = 30$ is appropriate.

Eq. 4.12 involves the inverse complementary error functions ($erfc^{-1}$), which is somewhat cumbersome. While many numerical packages (including Mathematica) compute it, a simpler analytic formulation of η is useful. Let $z = A m_X^2 / \alpha_{XXY} b_f C_{jj'}$. We find the approximation

$$\eta(z) \approx 1.978 - 0.521z - 0.051 log(z),$$

is almost exact in the range $10^{-8} \leq z \leq 1$.

Our analytic formula for a pole above threshold is now:

$$\Gamma_Y = \frac{1GeV}{4\pi\alpha_{XXY} b_f C_{jj'}} \left(\frac{m_Y}{589GeV}\right)^3 \left(1 - \frac{\eta(z) m_X}{m_Y}\right),$$

$$for\ m_Y > 2m_X. \tag{4.13}$$

Once again, the analytic approximation matches numerical work remarkably well. Fig. 4.8 shows an example.

Eq. 4.13 reveals more finely tuned parameter regions for a pole above threshold. In the limit $\Gamma_Y \to 0$, m_Y is finely tuned to ηm_X, as seen in Fig. 4.9. The competition between the pole position, width, and thermal Gaussian are all summarized by this generalization of the pole below-threshold relation.

As before, eliminating $\Gamma_Y = \alpha_\Gamma m_Y$ produces an $m_X - m_Y$ relation:

$$m_Y = \frac{\eta(z) m_X}{2} + \frac{1}{2}\sqrt{\eta^2(z) m_X^2 + 16\pi\mu^2 \alpha_\Gamma \alpha_{XXY} C_{jj'}},$$

where $\mu^2 = 589^3 GeV^2$.

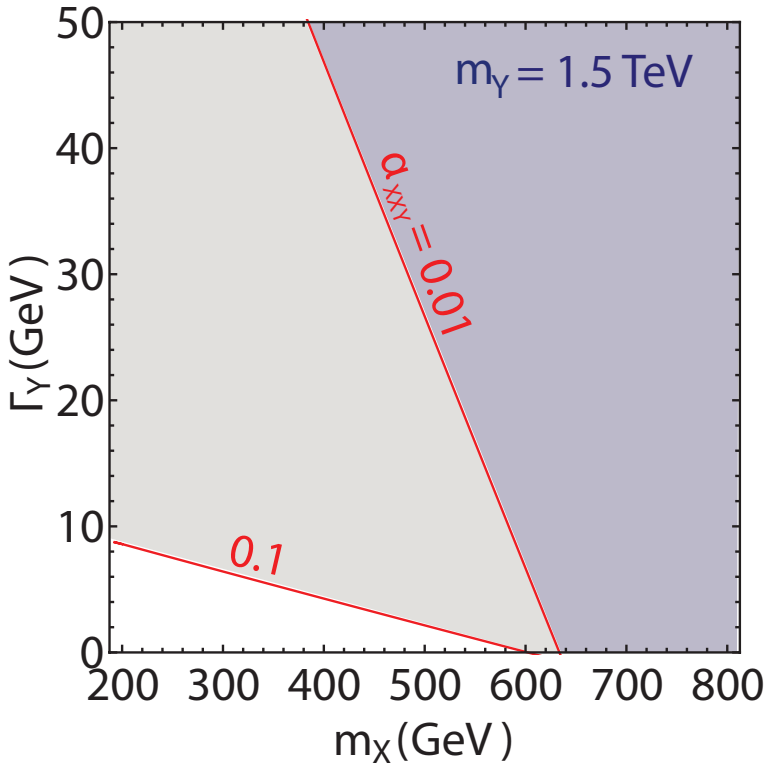

Figure 4.10: Typical upper limits on Γ_Y given a mass m_Y for different masses of dark matter m_X assuming both s-channel annihilation (pole above threshold) and other non-resonant channels. Shaded regions to the left and above the contours are not allowed. $m_Y = 1.5$ TeV was used for the purpose of the graphic; larger m_Y pushes contours to the right.

Upper Limit on m_X

The particular form of the "offset function" η yields an upper limit on m_X. From the derivation the argument of $erfc^{-1}$ must be less than one, which implies

$$m_X \leq 2.77 \times 10^5 GeV \sqrt{\alpha_{XXY} b_f C_{jj'}}. \tag{4.14}$$

This formula is more precise than supposing m_Y is bounded by a Born-level estimate and $2m_X < m_Y$. Consider for example a small coupling $\alpha_{XXY} b_f = 10^{-4}$. Consistency with relic abundance requires dark matter masses $m_X \lesssim 2.8 TeV$.

Inequalities for Non-Resonant Channels

Generalization of the above-threshold mass width relation to allow for non-resonant channels is similar to the below-threshold case. When $\langle \sigma v \rangle_{tot} \geq \langle \sigma v \rangle_s$ the mass width relation becomes

$$\Gamma_Y \leq \frac{1 GeV}{4\pi \alpha_{XXY} b_f C_{jj'}} \left(\frac{m_Y}{589 GeV} \right)^3 \left(1 - \frac{\eta\, m_X}{m_Y} \right). \tag{4.15}$$

An illustration of the inequality can be seen in Fig. 4.10. Notice that for large couplings, i.e. $\alpha_{XXY} b_f > 0.1$ major portions of the parameter space can be ruled out. The termination point ($\Gamma_Y \to 0$) is simply the $\eta m_X = m_Y$ point, giving us another bound on m_X. By inspection, a coupling $\alpha_{XXY} b_f = 0.1$ and $m_Y = 1.5 TeV$ requires $m_X \lesssim 600 GeV$.

Chapter 5

Constraints on Resonant Dark Matter Annihilation from Indirect Detection Experiments

As we already mentioned in Section 1.2, resonant dark matter annihilation drew much attention in the light of the recent measurements of charged cosmic ray fluxes. In considering dark matter annihilation in the galactic halo there are puzzles from comparing predictions of thermal relic densities with rates of particle production in the current era. In order to explain the PAMELA excess in positron fraction with a dark matter model, the annihilation cross section needed has to be orders of magnitude larger than the canonical $\langle \sigma v \rangle_0 \sim 10^{-9} GeV^{-2}$ of the WIMP miracle. In the literature, this is usually expressed via a "boost factor"

$$BF \equiv \frac{\langle \sigma v \rangle}{\langle \sigma v \rangle_0}. \tag{5.1}$$

The apparent contradiction between early universe and halo annihilation creates a need for a mechanism which allows for a small annihilation cross section in the early universe while enhancing the annihilation rate in the galactic halo. Since dark matter in the galactic halo is non-relativistic, the search for a viable enhancement mechanism has been largely focused in the threshold region $2m_X$.

Two popular classes of threshold enhancement mechanisms emerged:

In Section 3.2, we argued that dark matter annihilating through an s-channel resonance can produce thermally averaged cross section which increase as the universe cools down. Non-relativistic s-channel resonances can be motivated by either new particles or meta-stable bound states. Scattering amplitudes in non-relativistic scattering theory can be classified by their analytic properties in the complex momentum plane. Stable bound states are described by poles on the positive imaginary axis. It follows that stable bound states produce no remarkable enhancement of annihilation rates in the physical region of real momentum k. *Metastable particles* or *resonances*, described by poles of finite width, are in no way comparable with stable bound states, because everything observable (and potentially large) is a strong function of the width. We will discuss resonant dark matter in the context of halo annihilation in more detail in Section 5.2.

Threshold enhancements under the catch-phrase of "Sommerfeld factors" were also proposed [39, 55]. Sommerfeld factors are close cousins to s-channel bound state resonances, but there are significant differences in the dynamics which governs them. Often cited as "re-summations" of ladder diagrams, Sommerfeld factors serve as effective normalizations of asymptotic plane wave solutions in scattering theory, which take into account effects of long range interactions. As we show in Section 5.3 there are several, rarely discussed issues regarding Sommerfeld factors.

In this chapter, we will consider only constraints from indirect detection experiments. The consistency between thermal relic density and large boost factors in the halo is discussed in more detail in Chapter 6. Before we derive constraints on resonant dark matter annihilation from indirect detection, we proceed to first review in more detail the most important experimental contributions.

5.1 Experimental Searches for Dark Matter Signals in Charged Particle Fluxes

The Balloon borne Experiment Superconducting Solenoidal Spectrometer (BESS) experiment made several balloon flights and provided first measurements of anti-proton fluxes in the range of $200MeV$ to $3GeV$ [56]. The results confirmed a peak in the anti-proton flux at $\approx 2GeV$ as predicted by many cosmic ray flux models, while no anomalous signal that could be interpreted as dark matter was reported. Early measurement of the $4-50GeV$ anti-proton region was provided by the Cosmic Anti-Particle Ring Imaging Cherenkov Experiment (CAPRICE) [57]. No significant excess relative to background estimates was observed in the data.

The High-Energy Antimatter Telescope (HEAT) [18] measured positron fluxes in the region of $1-30GeV$. Although the uncertainties in the data were significant, the results showed an excess in positron fluxes relative to the galactic background starting at $\approx 10GeV$ and extending to higher energies. Subsequent flights of HEAT confirmed the signal [58].

The Polar Patrol Balloon (PPB) [17] and the Advanced Thin Ionization Calorimeter (ATIC) [19] made first accurate measurements of the electron fluxes in the region above $100GeV$. Both experiments reported an excess of five sigma in the $500-700GeV$ region relative to the galactic background. The authors of Ref. [19] were hesitant to interpret the excess as a result of dark matter annihilation, pointing to a possibility that a nearby dark object such as a pulsar could mimic the signal.

Perhaps the most interesting recent data came from PAMELA [15] and FERMI [16]. Both experiments measured an excess in the positron fraction in the region up to $100GeV$ to a high level of accuracy compared to previous experiments. The measured positron fraction was approximately 10 times larger than the expected background,

requiring dark matter interpretations of the signal to produce annihilation cross section orders of magnitude larger than the canonical $10^{-9} GeV^{-2}$. Dark matter was not the only possible interpretation as pulsars could also produce large enhancements in the positron fraction. [22–25]. Neither experiment reported an excess in the anti-proton flux up to approximately $100 GeV$.

It is important to address the apparent lack of a signal in anti-proton fluxes. Data tells us that if the excess in the charged lepton fluxes is due to dark matter annihilation, dark matter must not efficiently annihilate into quarks. This fact has to be taken into account on a model by model basis.

5.2 General Limits on the Resonant Velocity Averaged Resonant Cross Section in the Galactic Halo

In Section 2.3, we discussed the non-relativistic form of the resonant annihilation cross section, appropriate for the purpose of halo annihilation. The charged particle fluxes in the halo are dependent on non-relativistic form of the thermally averaged resonant annihilation cross section of dark matter, which we now develop.

The halo annihilation rate via a single $s-$wave resonance is governed by the velocity-weighted cross section $\langle \sigma v \rangle_{res}$ by

$$\begin{aligned} \langle \sigma v \rangle_{res} &= \int dv\, v \frac{4\pi v^N}{m_X^2 v^2} \\ &\times \frac{(\Gamma/2)^2 B_i B_f}{(m_X v^2/2 - m_X v_{res}^2/2)^2 + (\Gamma/2)^2} \Phi_{halo}(v). \end{aligned}$$

Here $\Phi_{halo}(v) = dN/dv^3$ is the normalized dark matter relative velocity distribution, assumed from astrophysics to be a smooth function on the scale of 100-500 km/s. In

an isothermal halo model the velocity distribution is in equilibrium,

$$\begin{aligned} \frac{dN}{d^3kd^3x} &= \frac{constant}{E_0} e^{-E/2E_0}; \\ \frac{dN}{dv} &= 4\pi \frac{v^2}{(2\pi v_0^2)^{3/2}} e^{-v^2/2v_0^2}. \end{aligned} \tag{5.2}$$

While the actual velocity distribution is uncertain, the phase space factors of v^2 are general. The isothermal halo will illustrate the method. Note however, that our upper bounds do not depend on the halo distribution.

The rate $\langle \sigma v \rangle_{res}$ is a function of E_0, E_{res}, Γ and m_X. If other scales are expressed in units of $m_X \sim TeV$ the conjunction of several rapidly varying functions makes analysis troublesome [36]. However in the present universe the halo energy $m_X v_0^2/2 \sim 10^{-6} m_X$ is rather small on particle physics scales. It is natural to rescale variables in units of the halo characteristic energy, defining

$$\gamma_0 = \frac{\Gamma}{2E_0}; \quad \delta_0 = \frac{E_{res}}{E_0}.$$

Assuming the equilibrium distribution, some algebra gives

$$\langle \sigma v \rangle_{res} = \frac{2^{2-N}(2\pi)^{\frac{N+1}{2}} v_0^{N-1}}{m_X^2} I_N(\gamma_0, \delta_0), \tag{5.3}$$

where

$$I_N(\gamma_0, \delta_0) = \frac{1}{2^{1-N}(2\pi)^{N/2}} \int_0^\infty dz\, z^{\frac{N}{2}} \frac{\gamma_0^2 e^{-z/2}}{(z-\delta_0)^2 + \gamma_0^2}. \tag{5.4}$$

Note that $I_N(\gamma_0, \delta_0)$ is analytic for all $\gamma_0 > 0$ and δ_0 regardless of the sign of δ_0. It can be computed exactly in terms of Exponential Integral (Ei) functions. We found it more useful to observe that $I_N(\gamma_0, \delta_0)$ has certain *absolute upper limits* for all possible

values of $\gamma_0 > 0$ and δ. Consider the derivative $\partial I_0(\gamma_0, \delta_0)/\partial\gamma_0$:

$$\frac{\partial I_0(\gamma_0, \delta_0)}{\partial \gamma_0} = \int dz \frac{2\gamma_0(\delta_0 - z)^2}{\left(\gamma_0^2 + (\delta_0 - z)^2\right)^2} e^{-z}. \tag{5.5}$$

Since the integrand above is positive definite, the integral achieves its maximum at $\gamma_0 \to \infty$. For $\gamma_0 >> 1$ the integration becomes trivial, yielding $I_N(\gamma_0, \delta_0) \leq 1$. A stronger limit notes the integrand of Eq. 5.4 is cut off for $z \lesssim \gamma_0$ when $\gamma_0 \lesssim 1$, $\delta_0 \lesssim 1$, implying $I_N(\gamma_0, \delta_0) \lesssim 1 - e^{-C\gamma_0}$, where C is a constant. Numerical work shows that for all parameters

$$\begin{aligned} I_0(\gamma_0, \delta_0) &\leq 1 - e^{-\frac{\pi}{2}\gamma_0}, \\ I_1(\gamma_0, \delta_0) &\leq 1 - e^{-\frac{\pi}{4}\gamma_0}. \end{aligned} \tag{5.6}$$

These are close to equality for positive $\delta_0 << 1$. Fig. 5.1 shows a plot of $I_N(\gamma_0, \delta_0)$for a wide range of γ_0, δ_0 and how the integral approaches the upper bound.

The positivity property of Eq. 5.5 holds for all halo distributions. The upper limit $BW \to 1$ produces a universal inequality:

$$\langle \sigma v \rangle_{res} < \frac{4\pi \langle 1/v^{1-N} \rangle}{m_X^2}. \tag{5.7}$$

The expected value $\langle 1/v \rangle$ is relative to the distribution $\Phi_{halo}(v)$, not dN/dv. If the equilibrium distribution is assumed, then

$$\langle \sigma v \rangle_{res} < \frac{2^{2-N}(2\pi)^{\frac{N+1}{2}} v_0^{N-1}}{m_X^2}(1 - e^{-\pi\gamma_0/2^{N+1}}). \tag{5.8}$$

The result is a significant enhancement factor (EF) ("boost factor") for annihilation rates. The enhancement factor is defined relative to a typical Born approximation

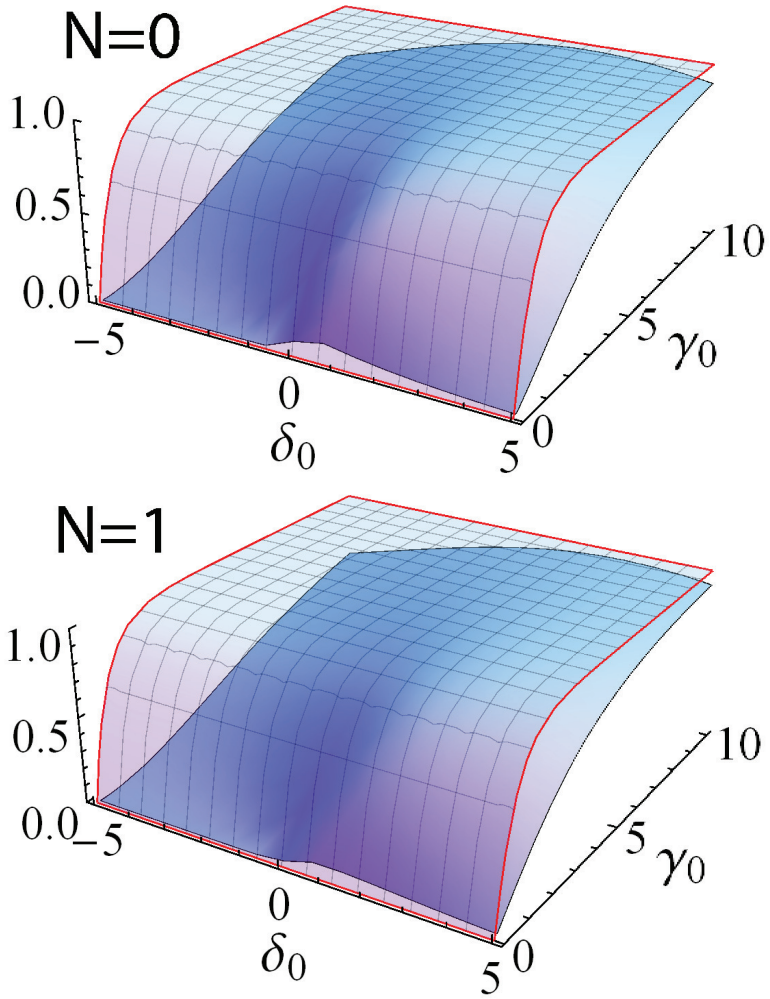

Figure 5.1: The integral $I_N(\gamma_0, \delta_0)$ (dark shaded) and upper limits cited in the text (transparent mesh). By Eq. 5.3 the rate constant is related via $\langle \sigma v \rangle_{res} \sim v_0^{N-1} I_N / m_X^2$.

$\sigma_{Born} = 4\pi\alpha_X^2/m_X^2 v^{2-N}$:

$$EF = \frac{\langle \sigma v \rangle_{res}}{\langle \sigma v \rangle_{Born}} \leq \frac{1}{\alpha_X^2}. \tag{5.9}$$

Note that the inequality does not depend on the position of the resonance nor on any halo properties.

$N = 0$ Enhancement Factors

For $N = 0$, Eq. 5.9 leads to substantial enhancements approaching the unitarity bound when the fundamental width Γ is large enough. Obtaining a "large enough" width from a weakly coupled theory might appear special. Yet remember that halo annihilations are driven by the width in units of the rather small scale $E_0 \sim 10^{-6} m_X$. For TeV-scale dark matter a width $\Gamma \gtrsim$ MeV is large enough to dominate the halo width and make $BW(\Gamma, E_{res}) \sim 1$. Recall that the J/ψ has a width of order 0.1 MeV and is exceedingly "narrow". For an elementary particle on any mass scale of GeV-TeV *not to have* widths exceeding $10^{-6} m_X$ requires special conspiracies or selection rules. As shown in Fig. 5.2, even a tiny value of $\Gamma/m_X \sim 10^{-8}$ can produce rates much larger than the oft-cited value $\langle \sigma v \rangle \sim 3 \times 10^{-26} cm^3/s$. It is a new insight that merely including physics of widths tends to saturate unitarity bounds in halo annihilation.

$N = 1$ Enhancement Factors

Equation 5.7 highlights a factor of $\langle 1/v \rangle$ absent with a relativistic phase space ($N = 1$). To a first approximation the ratio of the $N = 1$ case relative to the $N = 0$ case is of $O(v_0)$. This is made more precise using Fig. 5.3, which shows a plot of the calculated ratio of integrals I_1/I_0 that remains. This ratio is of order unity for most of the parameter

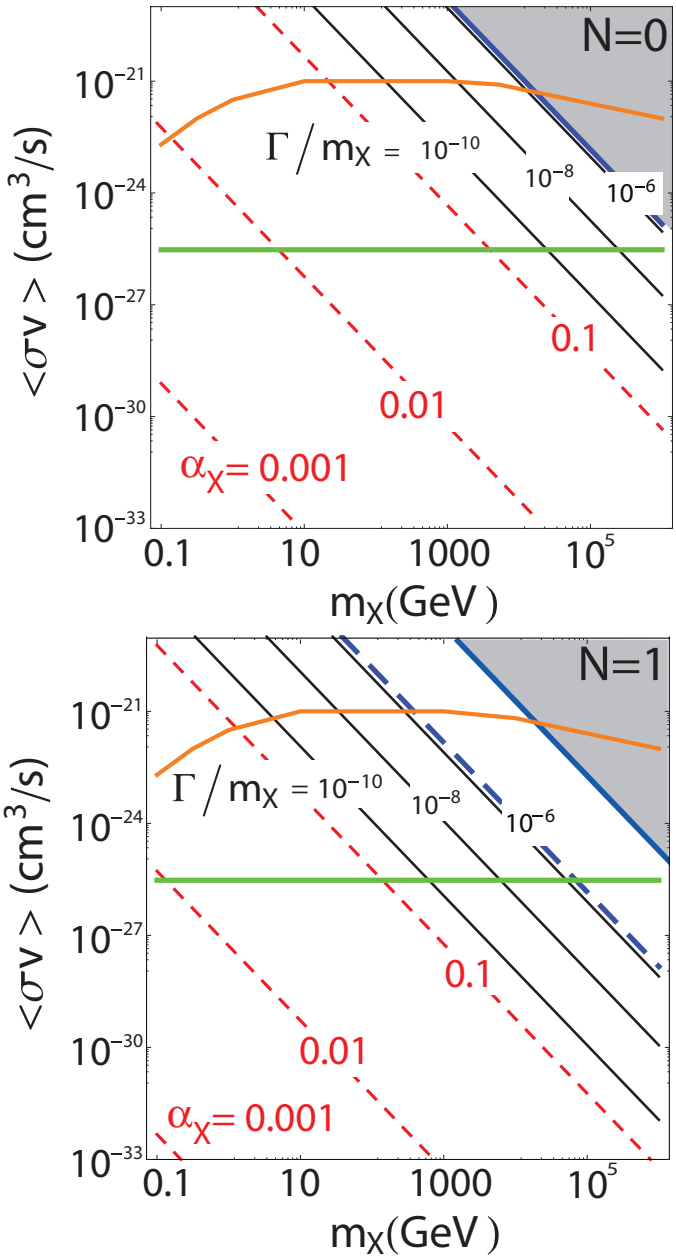

Figure 5.2: Upper limits (diagonal lines) of resonantly enhanced annihilation rate $\langle \sigma v \rangle_{res}$ in the isothermal halo distribution. Solid curves (black) are computed with fixed Γ/m_X. Gray triangle in upper right the unitarity bound. The thick dashed curve (blue) is the maximum value for the cross section for $N = 1$. Thin dashed curves (red) show $\langle \sigma v \rangle_{res}$ computed for bound state processes using $\Gamma = \alpha_X^5 m_X/2$ and $E_{res} = -m_X \alpha_X^2/4$. Middle curve (orange) is the neutrino-based upper limit of Ref. [59]. Horizontal line (green) is a conventional lower bound $\langle \sigma v \rangle \sim 3 \times 10^{-26} cm^3/s$.

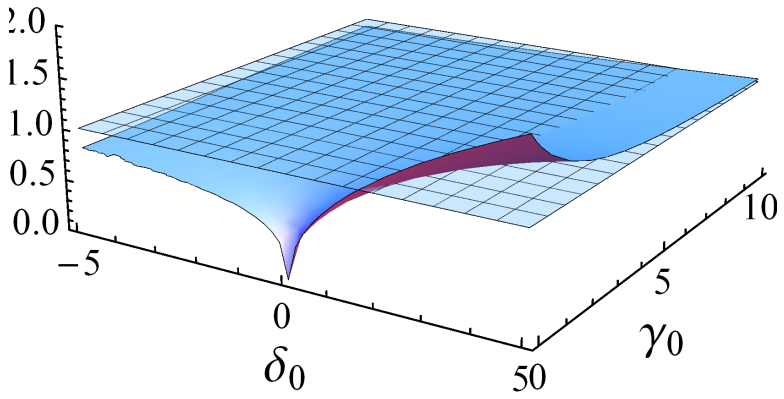

Figure 5.3: Ratio of I_1/I_0 (shaded area) compared to the uniform value of 1 (mesh).

space, except the regions where $\gamma_0 << 1$. Once again, only when widths are very tiny do resonance widths *not* tend to swamp the halo distribution.

While representing stronger limits, the bottom panel of Fig. 5.2 again shows significant enhancements over a broad range of parameters of current interest. The difference between the $N = 0$ and $N = 1$ cases tends to disappear whenever Γ/m_X is not exceptionally small. In the next Section we turn to the metastable bound state case, which does happen to exhibit exceptionally small widths on general grounds.

5.2.1 Metastable Bound States, and Narrow Resonances

The case of annihilation passing through intermediate metastable bound states has generated great interest. This case is different and deserves a separate discussion. Suppose dark matter interacts with a light messenger particle of mass μ, with coupling-squared α_X. If the interaction is attractive, which is readily arranged for particular spins, then non-relativistic physics predicts *there is always a bound state* for sufficiently large cou-

pling. The conditions are

$$\alpha_X \geq \kappa \frac{\mu}{m_X},$$

where κ is a constant of order one. The demonstration is an easy variational calculation using a ground state Hydrogenic wave function. A helpful discussion is also given in Ref. [52]. For parameters $m_X \sim TeV$ and $\mu \sim GeV$ bound state formation needs $\alpha_X \gtrsim 10^{-3}$, which is well within the electroweak-scale couplings of most models.

Yet just as above, everything about any significant enhancement depends strongly on the *width*, and won't proceed without it. To estimate widths, first note that bound states are spatially large for small coupling constant α_X. The size of a weakly coupled bound state is roughly estimated by the "Bohr radius" a_0, where

$$a_0 \sim 1/m_X \alpha_X.$$

Similarly, the binding energy $E_{res} \sim m_X \alpha_X^2$. Next recall that the Schroedinger wave function at the origin $\psi(0)$ determines the width via $\Gamma \sim |\psi(0)|^2 \sigma_c$ where σ_c is a continuum cross section. The wave function at the origin is set by the inverse of the size of the bound state:

$$|\psi(0)|^2 \sim a_0^{-3} \sim \alpha_X^3.$$

The continuum annihilation cross section $\sigma_c \sim \alpha_X^{1+A}$ for $A > 0$ depending on the model. For reference the annihilation rates of ortho (para) positronium via three (two) photons go like $\alpha_{em}^6 (\alpha_{em}^5)$. Thus bound state widths go by a general pattern

$$\Gamma \sim \alpha_X^{4+A} m_X \lesssim 10^{-8} m_X.$$

The right hand side is a fair upper limit for $\alpha_X \sim 10^{-2}$. Restricted phase space factors and branching ratios can only reduce this. Comparing $E_0 \sim 10^{-6} m_X$, we find that $\gamma_0 << 1$ is by far the generic case for annihilation from a bound state. As a consistency check, consider the definite case of spin-1/2 dark matter interacting with vector particles. Nature has already done this calculation with the J/ψ decay via gluons, which has $\Gamma_{J/\psi}/m_{J/\psi} \lesssim 10^{-4}$. The J/ψ is sufficiently heavy that the perturbative phase space factors are driven by dimensional analysis, as expected for TeV-scale physics. The raw J/ψ ratio needs to be re-scaled by $(\alpha_X/\alpha_s)^{4+A} \sim 10^{-4}$, which gives satisfactory agreement.

When $\gamma_0 << 1$ it is a good approximation to replace $BW(\Gamma, E_{res}) \sim \pi(\Gamma/2)\delta(E - E_{res})$. A short calculation then gives

$$EF(\gamma_0 << 1) = \frac{\pi\Gamma/2}{\alpha_X^2 m_X v_{res}^{2-N}} \frac{\Phi_{halo}(v_{res})}{\left\langle \frac{1}{v^{1-N}} \right\rangle}, \tag{5.10}$$

where $E_{res} = m_X v_{res}^2/2$. This formula has no singularity as $v_{res} \to 0$ because $\Phi_{halo}(v_{res}) \sim v_{res}^2$ has compensating factors from phase space (Eq. 5.2). If a metastable bound state resonance lies *above threshold* in an expected electroweak range the effects are quite small. Taking $E_{res} = m_X \alpha_X^2/2 \sim 10^{-4} m_X$, and the equilibrium halo model with scale $v_0 = 10^{-3}$, the factor $e^{-E_{res}/E_0} \sim e^{-100}$ is too small to consider further. When the resonance is *below threshold* it must have width $\Gamma \gtrsim |E_{res}|$ to intrude into the physical region. Since Γ is proportional to several powers of α_X compared to E_{res} this case can also be set aside. If $E_{res} \to 0$ with $\Gamma >> E_{res}$ is contemplated, it implies the decay time scale is much less than a binding (orbital) time scale, which is not consistent with bound states forming in the first place.

The exponentially small suppression can be avoided by adjusting the coupling into the range probed by the halo velocity. For example choose $\alpha_X \sim 10^{-3}$. This device

rapidly loses consistency because the bound state criterion $\alpha_X \gtrsim \mu/m_X$ needs couplings not too small. If a bound state is tuned to the vicinity of the peak, then the halo factors will be of order unity. Meanwhile there remains in Eq. 5.10 an overall factor of $\Gamma/(m_X \alpha_X^2) << 1$. Fig. 5.2 compares the upper limits from annihilation of continuum processes ($\gamma_0 \gtrsim 1$ generically) to processes proceeding via the bound state ($\gamma_0 \lesssim 10^6 \alpha_X^5$) using the isothermal halo and conservative values $B_i B_F \to 1$. Viable enhancement mechanisms should also respect the neutrino-based bounds of Mack, Beacom and Bell [59] included in the Figure. In case of $N = 0$, a bound state could cause large cross section enhancements, but only for couplings $\alpha_X \geq 0.1$ which are beyond the stable perturbative regime. In case of $N = 1$ the limits for bound states are even tighter.

Fig. 5.2 shows that a single bound state with perturbative couplings has no chance of causing significant enhancements. Except for strong coupling, there is *no dynamical mechanism to generate large enhancement factors from non-relativistic bound state resonances in the current universe.* The conclusion does not depend on the spin or quantum numbers of new physics, and is too strong to escape by adding up several resonances, unless they are so numerous their numbers alone overcome small couplings, as for KK modes.

5.2.2 Comparisons with Previous Work of Resonant Dark Matter Annihilation in the Galactic Halo

Ibe, Murayama, and Yanagida [60], and Guo and Wu [61] focus on calculating thermal evolution for the case of a state just below threshold. In their model the width is proportional to the final state velocity (equivalent to $N = 1$). The resonance position is close enough to threshold for its effects to overlap into the physical region

during evolution. They find that even a tiny ratio of width to resonance invariant mass, denoted by $\gamma = \Gamma/M_{res} \lesssim 10^{-3}$, produces significantly larger relic densities than traditional constant cross section approximations. To keep the relic density Ω_X fixed, avoiding over-closure, parameters must then be adjusted to produce relatively larger cross sections. We will discuss the consistency between large boost factors in the halo and relic abundance further in Chapter 6.

Our emphasis is annihilation rates observed in the present universe. This is determined by $\gamma_0 = \gamma(M_{res}/2E_0)$ rather than Γ/M_{res}. Since they are based on Γ/M_{res}, which has no halo information in it, the boost factors of Refs. [60], [61] do not capture the Breit-Wigner effects of the halo. Instead, the *assumed* halo boost factors for constant cross sections were estimated from the re-scaling factors keeping Ω_X fixed. The implications of those boost factors that very small Γ/M_{res} is necessary or tends to enhance halo rates are not general. Despite this problem, a window exists that significant halo rate enhancements will be present over a broad compatible range $10^{-3} > \Gamma/m_X > 10^{-6}$.

5.3 Sommerfeld Factors

In the previous section, we have shown that Breit-Wigner width effects of typical particle physics type can be surprisingly large, while bound state effects have little chance to compete. Sommerfeld factors have also been claimed as a mechanism of large halo enhancements not involving particle widths [39]. In the scenario where non-relativistic dark matter particles are allowed to interact through massless t-channel exchanges, the Sommerfeld factors are usually defined as

$$S(v, \alpha) = \frac{\alpha}{v} \frac{2\pi}{1 - e^{-2\pi\alpha/v}}. \tag{5.11}$$

There are several issues with the motivation and derivation of Eq. 5.11, which we discuss in much detail in this section.

Sommerfeld factors are often cited as non-perturbative re-summations of ladder diagrams [40, 62, 63]. In Section 5.3.1, we show that wave function normalizations used in Sommerfeld factors can not in principle be equivalent to ladder diagram re-summations in all kinematic regions. In addition, we point out that the approximations assumed in Sommerfeld factors break down in the exact kinematic regions where large enhancements are expected.

Actual derivation of Sommerfeld factors and consistency checks with general scattering theory is typically absent from the literature. Hisano et. al. [40] offer a rare detailed derivation of Sommerfeld factors. We discuss their work further in Section 5.3.2.

Notice that $S(v, \alpha)$ has a threshold ($v \to 0$) singularity. In Section 5.3.3, using partial wave unitarity, we show that threshold singularities can not be generated by multiplicative factors such as $S(v, \alpha)$ for any individual partial wave. To generate a singularity of this type, we show that a sum of infinite number of partial waves is required.

5.3.1 Motivation for Re-summation

Non-relativistic *QED* has complicated logarithmic and power-behaved infrared singularities. The Sommerfeld factor is associated with re-summing an infinite series [64] in (α^j/v^k) selected by matching $j = k$. Here α is the fine structure constant. By definition sub-leading terms are dropped. These terms are higher order in α for a given power of $1/v$. Since it is always possible to add a photon exchange loop to any diagram, and

all loops have some integration region *not* singular as $v \to 0$, sub-leading terms always exist, in huge variety.

Sommerfeld prescriptions hold that the leading singularities appear as follows[1]. Given an $s-$wave cross section σ_0, which has been computed with plane waves, the Sommerfeld-based recipe to include Coulomb wave effects is

$$\sigma_0 \to \sigma_{GS} = \sigma_0 S(v, \alpha), \tag{5.12}$$

where $S(v, \alpha)$ was defined in Eq. 5.11. In modern parlance the formula is a leading-order, leading power factorization, as explained momentarily.

Some examples illustrate the function and limitations of re-summation. Expand $S(v, \alpha) \sim 1 + \pi(\alpha/v) + \pi^2\alpha^2/3v^2 + \ldots$. For $\alpha = 10^{-2}$, and $v = 5 \times 10^{-2}$ the third term is $\pi^2/75 \sim 0.13$. It is larger than a typical non-singular term of order α, and retaining it is motivated and credible. The series is also stable, as a high order term $(\pi\alpha/v)^{10} \sim 0.0096$ is small. A sub-leading term $\alpha^{11}(\pi/v)^{10}$ is 100 times smaller, and negligible. But at $v = 5/1000$, the neglected sub-leading correction $\alpha^{11}(\pi/v)^{10} \to 958956.0$ is hardly negligible. One should not imagine that corrections should be straightforward: after powers of v are managed, there are generally infinitely many powers of $log(v)$. Self-consistency breaks down in the region $\alpha/v \gtrsim 1$, exactly where $S(v, \alpha) \gtrsim 1$.

Yet recent treatments of dark matter annihilation have imagined the Sommerfeld factor to be very general, and responsible for large enhancement factors of $S >> 1$ from any interaction involving light Yukawa particles [66]. The perception comes from identifying the leading order Sommerfeld factor with continuum Coulomb normalization factors $|\psi_C|^2(0)$. Then since $\psi_C(0)$ is known exactly, the procedure has been thought "exact." There are many logical and historical contradictions. First, Guth and Mullin

[1] Many papers, e.g. Ref. [65] quote results without derivation or approximations. We have not actually found a proof in the literature.

had already highlighted the approximations in 1951 [67]. *In lowest order approximation*, but while using Coulomb wave functions ψ_{Ci} for a basis, one encounters matrix elements M of the form

$$M = \int d^{3x}\, \psi^*_{C2} V \psi_{C1}.$$

Insert complete sets of momentum eigenstates $|k\rangle$:

$$M = \int d^3k\, d^3k'\, \psi^*_{C2}(k) V_{kk'} \psi_{C1}(k').$$

The Coulomb wave functions are sharply peaked in the vicinity of certain momenta k_1, k_2, identified by taking the limit $\alpha = 0$. Assume the plane-wave matrix elements $V_{k_1,k_2} = \langle k_1|V|k_2\rangle$ are relatively smooth functions of momentum transfer. Make a rough approximation moving $V_{k_1 k'_2}$ outside the integral:

$$\begin{aligned} M &\rightarrow V_{k_1,k_2} \int d^3k\, \psi^*_{C2}(k) \int d^3k'\, \psi_{C1}(k), \\ &\rightarrow V_{k_1,k_2} \psi^*_{C2}(x=0) \psi_{C1}(x=0). \end{aligned}$$

In the last line $\psi_C(x=0)$ appears as the coordinate-space wave function at the origin, "improving" the plane wave calculation. This is just the same factorization approximation of separating "hard" and "soft" regions of leading power perturbation theory, without even attempting control of corrections. Careful work with positronium annihilation [68] is done by avoiding the factorized approximation. The authors [68] recognize that "Coulomb effects are included by this (factored) method to all orders in e^2, *though only, of course, approximately*." (Italics are ours.)

What did Sommerfeld actually do? His 1931 article, in German, introduced exact Coulomb wave functions to calculate bremsstrahlung, but never suggested factoriza-

tion. While a *tour de force* of early quantum theory, consulting it for a renormalization factor actually perpetuates a normalization mistake. The overall normalization of physical states cancels out in total cross sections. Cross sections are defined by ratios relative to a flux computed with given normalization. Elwert's 1939 dissertation [69, 70] recognized this, as as did Guth in 1941 [71]. These papers abandoned Sommerfeld's calculation and used the *ratio* of two in- and out- Coulomb factors as an approximate factorized ansatz. "Elwert factors" are used in atomic and molecular physics to cancel spurious pre-factors going like v from other approximations and only when their effects are not too large. Experimental confrontation of the Elwert factor finds errors of relative order unity in the region where the factors are of order unity [69, 70, 72]. Elwert and collaborators find breakdown reasonable [69, 70], and in no event are very large corrections ever credited. The history is scant in particle physics because superficial citation of Sommerfeld cut the links to the main literature on the subject.

5.3.2 A Derivation of Sommerfeld Factors

It appears that derivations of Sommerfeld Factors in dark matter physics typically involve assuming the answer beforehand. Hisano et. al. [40] provided a very detailed and often cited derivation of the re-summation implied in the multiplicative Sommerfeld enhancement

$$\sigma = S\sigma_0, \tag{5.13}$$

where σ_0 is the Born level cross section and S is the Sommerfeld factor. However, the mechanism through which the authors of Ref. [40] seem to generate enhancements is quite different from Eq. 5.13 and the validity of the derivation is flawed for a number of reasons which we now discuss.

After starting with a relativistic, hermitian field theory, the authors reduce the problem to beginning quantum mechanics. The method of reduction is presented as a substitution of the desired answer after stating that different degrees of freedom of the relativistic theory are integrated out. The actual threshold enhancement is motivated by solving the Schroedinger Equation for the non-relativistic Green's function and evaluating the amplitude, which is in no way similar to attaching a form factor to a Born-level cross section. A crucial step in the derivation is the replacement of all the interactions in the theory with a complex potential

$$V'(\vec{r}) = V(\vec{r}) + i\Gamma\delta(\vec{r}). \tag{5.14}$$

There seems to be a discontinuity in the derivation once Eq. 5.14 is introduced. None of the previous work in the paper was used to motivate the effective potential of Eq. 5.14. The authors start with a Hermitian theory, which somehow turns into a non-Hermitian one once the interactions are replaced by a complex potential. Knowing this, the paper might as well begin with the non-Hermitian effective hamiltonian. The use of complex potentials is nothing new, but Hamiltonians with complex potentials are used only as phenomenological tools to fit data, with no real predictive power. The action of Eq. 5.14 is equivalent to the statement "there exists a resonance," which means that a pole was planted into the theory before hand. It did not appear as a consequence of the derivation.

Replacing interaction terms with the complex potential of Eq. 5.14 is not "illegal", but it is under no circumstances a "universal" prescription. Also, generating threshold singularities through the use of complex potentials is in principle completely different from the multiplicative rule $\sigma \to S\sigma$

The mechanism of threshold enhancements employed in Ref. [40] is by no means exact either, as there are a number of questionable steps involved. The authors integrate out the gauge bosons to obtain the effective action. The approximation of the interaction terms with the green's functions is one of classical physics and there is no explanation why such a step is valid. As a result, any claim about the inclusion of all possible terms of the effective action is invalid. Finally, replacing the entire relativistic, *hermitian*, field theory with Eq. 5.14 which contains a complex potential, makes the time evolution of the model non-unitary. Eq. 5.14 cannot in principle exactly follow from any previous calculation in the Ref. [40]. Resonances and the effects of bound states orthogonal to the continuum do not in general appear as imaginary delta function potential terms in Schroedinger theory. The exact formalism is formally Hermitian, but inherently non-local in time. All approximations made by Hisano et. al. discard any possible non-local terms.

5.3.3 Multiplicative Factors Must Fail

The concept behind generating singularities via multiplicative factors is incorrect on general grounds. The reasons are simple yet overlooked due to gaps in literature.

A general scattering amplitude has the partial wave expansion

$$f(\theta,k) \quad = \quad \frac{1}{k}\sum_{l}(2l+1)f_l(k)P_l(cos\theta).$$

For each partial wave cross section σ_l of angular momentum l, elastic unitary gives the upper limit

$$\sigma_l = \frac{4\pi(2l+1)|f_l(k)|^2}{k^2} \leq \frac{4\pi(2l+1)}{k^2}.$$

This summarizes the unitarity bound of Ref. [73]. Since each partial wave has a finite cross section, *no partial wave can possibly have a singularity*. "Improving" the s-wave cross section - or any particular partial wave cross section - by singular terms of order α_X/v then contradicts unitarity for $\alpha_X/v \gtrsim 1$. This is just the same region where the claimed Sommerfeld factor $S(v, \alpha) >> 1$.

It is not possible to escape the contradiction by appealing to small α_X. No special value for α_X was specified in developing the Sommerfeld-cited argument: it is based on "exact" normalization. Small coupling is also no protection from internal inconsistency. Unitarity and analyticity in perturbation theory are exact facts maintained in a systematic way, order by order, regardless of the size of the coupling constant, small or large. When violated, it shows the re-summation was bad, just as suggested by sub-leading terms that were dropped[2].

This problem is different from the one previously recognized. Dark matter interactions have finite range, while the infrared singularities of re-summation come from infinite range. To account for this the authors of Ref. [39] argued that for a finite range potential, a non-resonant enhancement would saturate when the deBroigle wavelength of colliding particles would be larger than the range of the force (i.e. $v < \mu/m_X$). Note that this criterion does not depend on any coupling constant. Yet the singularities of scattering amplitudes, and particularly Coulomb singularities, do depend on the coupling. Whatever the scale where analogies between massless and massive models break down, the facts of partial wave unitarity are more general, and take precedence. Unitarity precludes large enhancement in every particular channel of fixed angular momentum.

[2]Work by Cassel [66] and Iengo [66] seek normalization pre-factors of the form $\sigma_l \to \sigma_l S_l$ from the start. Those assumptions then contradict unitarity, as Cassel noticed.

Since each partial wave is finite, how do some Coulomb-dominated processes, such as Rutherford scattering, actually become singular as $v \to 0$? The answer leads to another useful bound. Replace every partial wave by the one with largest magnitude $|f_{max}|^2 = 1$. Sum them up to an order l_{max}: The result is

$$\sigma \leq \frac{4\pi}{k^2} \sum^{l_{max}} (2l+1) = \frac{4\pi(l_{max}+1)^2}{k^2}.$$

This is a strict upper limit. The Sommerfeld factor is not a resonance, and in the absence of resonances $|f_{max}|^2$ for every partial wave is small in weakly coupled theories, making σ small. The notion of canceling a perturbative factor of α_X^2 with an enhancement of 10^4 (say) needs $l_{max} >> 10^2$ partial waves. This is highly unlikely, since the angular momentum involved in annihilation is strictly limited by the quantum numbers of intermediate states, seldom consisting of more than a few elementary particles.

As Wigner [74] and many others have noted, the Coulomb singularity itself is very special. On semi-classical grounds (actually the facts of Legendre series), the upper limit $l_{max} \sim r_{max}k$, where r_{max} is the range of the potential. Take l_{max} to be a very large number. This gives

$$\sigma \leq 4\pi r_{max}^2 |f_{max}|^2 = 4\pi r_{max}^2.$$

The Coulomb singularity occurs because (1) the effective range $r_{max} \to \infty$, and (2) an infinite number of partial waves do contribute. Closely related is Wigner's classic theorem [74] that power-law potentials $V(r) \gtrsim 1/r^2$ are needed to develop any kind of singularity.

Chapter 6

Combined Constraints from Relic Abundance and Indirect Detection

A combination of halo constraints and relic abundance allows for a new set of limits on dark matter masses and couplings. In order to explain the halo positron excess with a dark matter model, an annihilation cross section enhancement, or boost factor, of order $BF \sim 100 - 1000$ is needed. In Chapter 5 we argued that such large boost factors are possible for dark matter annihilating through an s-channel resonance. Requiring simultaneously $BF \sim 100$ in the halo and the correct relic abundance allows us to put an upper limit on dark matter mass given the coupling of dark matter to the resonance and vice versa. In order to derive the new limits, we begin with scaling relations discussed in the next section.

6.1 Useful Scaling Relations

A textbook-style relic abundance scaling law states that for a velocity averaged cross section

$$\langle \sigma v \rangle = \frac{\alpha_X^2}{m_X^2}, \tag{6.1}$$

the relic abundance will scale as

$$\Omega h^2 \sim m_X^2/\alpha_X^2, \tag{6.2}$$

where α is some effective dimensionless coupling.

As we will show momentarily, it is important to note that the product

$$\langle \sigma v \rangle \times \Omega h^2 \neq f(m_X, \alpha_x). \tag{6.3}$$

Eq. 6.3 is particularly useful, since it allows us to reduce any multidimensional parameter space by eliminating dependence on m_X and α_X. Reducing parameter spaces to fewer dimensions can in effect greatly simplify both analytic and numerical analysis.

It is possible to extend Eq. 6.3 to dark matter annihilation scenarios beyond the simple Born approximation. As it turns out, the function f contains crucial information needed to derive new limits on dark matter masses and couplings, which we now develop.

To illustrate, we use our general form of the resonant cross section in Eq. 2.5 [1].

Consider the case $m_Y \sim 2m_X$. Then $t_{jj'} \sim m_Y^2$ and the velocity averaged cross section can be cast into the form

$$\langle \sigma v \rangle = \frac{g_{XXY}^2}{m_X^2} BW(\Gamma_Y, m_Y, x), \tag{6.4}$$

where BW is the Breit Wigner form factor. The relic abundance will then take the form

$$\Omega h^2 = \frac{m_X^2}{g_{XXY}^2} \omega(\Gamma_Y, m_Y). \tag{6.5}$$

[1] It is straightforward to generalize the argument to any velocity averaged cross section where the dependence on the coupling and the mass of dark matter can be effectively factored out.

The product of Eq. 6.4 and Eq. 6.5 is then

$$\frac{\langle\sigma v\rangle(x)}{\langle\sigma v\rangle_0} \times \Omega h^2 = f(\Gamma_Y, m_Y, x), \tag{6.6}$$

where we can write $x = m/T \approx 1/v_0^2 \approx 10^6$ in the halo. In the last step, we rescaled $\langle\sigma v\rangle$ by the canonical cross section $\langle\sigma v\rangle_0 \sim 10^{-9} GeV^{-2}$ in order to obtain a dimensionless product f. Taking $x = 3 \times 10^6$ in Eq. 6.6 represents the product of the boost factor in the galactic halo and the relic abundance. Again, notice that f does not *explicitly* depend on the mass of dark matter or the coupling g_{XXY}.

What useful information can we extract from Eq. 6.6? Assume that f has already been calculated. Requiring $\Omega h^2 \sim 0.1$ then gives

$$BF \approx 10 f(\Gamma_Y, m_Y, 3 \times 10^6). \tag{6.7}$$

Eq. 6.7 gives us a relationship between the boost factor BF required in the halo for a given resonance mass m_Y, width Γ_Y and the correct relic abundance. A plot of Eq. 6.7 as a function of rescaled dimensionless variables

$$\gamma' = \frac{\Gamma_Y}{m_X}, \qquad \delta' = \frac{2m_X - m_Y}{m_X}, \tag{6.8}$$

can be seen in Fig. 6.1 for a pole below threshold. The color map represents the increase in the required boost factor from lower (dark) to higher (light). It is clear from the plot that consistency with relic abundance allows for large boost factors only in the regions of small δ, γ. For instance, in order for the parameter set $\gamma = \delta = 10^{-4}$ to give correct relic abundance, the boost factor in the halo should be of $O(10)$. The assumption of the correct relic abundance is crucial in this statement.

Notice that Eq. 6.7 gives only the enhancement assumed to occur at $x = 3 \times 10^6$. *The calculation does not guarantee that the enhancement will be achieved,* because it was computed under the assumption that $\Omega_{DM}h^2 = 0.1$ for all γ, δ. There are two independent calculations which must be reconciled to proceed.

Consider a pair of values $\gamma^* = 10^{-3}$, $\delta^* = 10^{-3}$. Eq. 6.7 then predicts the cross section *needs to be* $\langle\sigma v\rangle \approx 100 \times \langle\sigma v\rangle_C$ at $x = 3 \times 10^6$ for relic abundance to be consistent. Desire for the boost factor to have this value, however, does not mean a calculation has yet given it. This fact has previously been overlooked. Information about the dependence of Ω_{DM} and $\langle\sigma v\rangle$ on mass, couplings, etc. is necessary for the argument to proceed. That is just the information we have developed with Fig. 6.2.

6.2 Previous Considerations of Simultaneous Relic and Halo Constraints on Resonant Dark Matter Annihilation

Refs. [60, 61] contain plots very similar to the one in Fig. 6.1. However, the authors interpret the results as the *actual* rather than the *desired* boost factors. This interpretation cannot possibly be accurate, as the resonant cross section is a function that depends on more than the width and the resonance mass. Cross sections are also explicit functions of couplings and the mass of dark matter. Demanding a certain magnitude of the boost factor, Fig 6.1 can give limits on the mass of the resonance and the width relative to the mass of dark matter. For instance, if we demand $BF \geq 100$ it is clear that we must choose parameters in the region $\delta' \leq 10^{-4}, \gamma' \leq 10^{-3.5}$. However, knowing the limit on the width and the mass of the resonance simply does not contain enough information to actually predict the boost factor in the halo. Essential information about the depen-

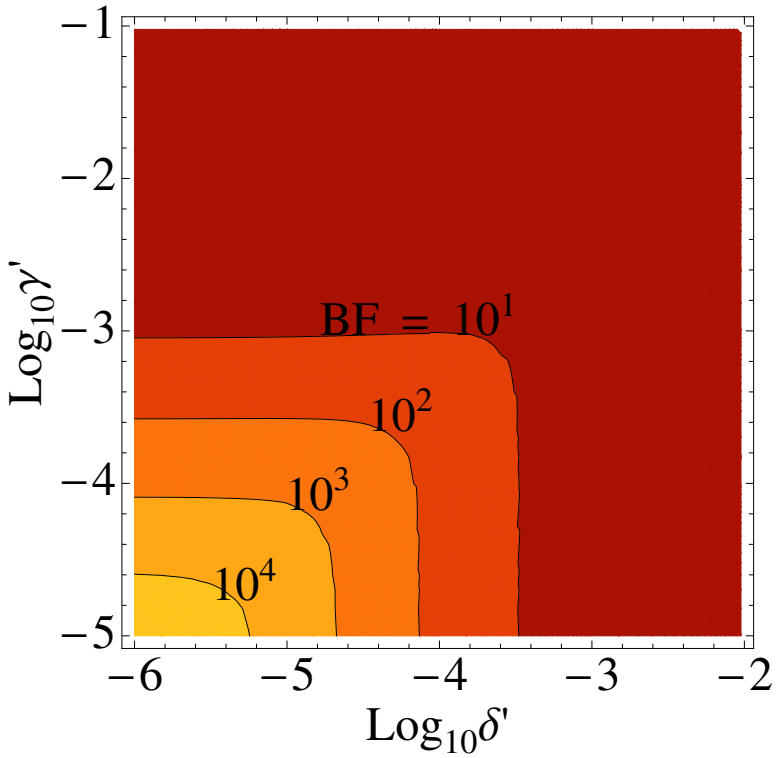

Figure 6.1: Desired boost factor in the galactic halo as a function of the rescaled width $\gamma' = \Gamma_Y/m_X$ and the distance of the resonance mass from the threshold $\delta' = (2m_X - m_Y)/m_X$. Different contours represent a constant value of the boost factor BF in the halo. Boost factors of $O(100)$ or more are achievable only for $\delta' \leq 10^{-4}$ and $\gamma' \leq 10^{-3.5}$.

dence of the boost factor on the mass of dark matter and the coupling g_{XXY} is absent from Fig. 6.1. In the next section, we take into account a full set of parameters to derive new limits on dark matter masses and couplings.

6.3 Dark Matter Mass and Coupling Limits

In the previous section we have shown that the information in Eq. 6.7 is not sufficient to predict large boost factors in the galactic halo. Instead, Eq. 6.7 provides us with a desired boost factor, given correct relic abundance, but doesn't guarantee that such a boost factor is achievable. To determine whether large boost factors are possible at all, we must add information about the other relevant parameters such as the mass of dark matter and couplings. Given the interest in recent positron excess data from indirect detection experiments, we illustrate our calculations using $BF \geq 100$.

Boost factors of any particular size are not guaranteed by stating how big we'd like them to be. The further conditions of Eq. 6.7 produce the real restrictions. Using a complete set of parameters, here we develop a new bound on the mass of dark matter by combining the joint information from indirect detection and relic abundance.

We proceed as follows. Contours of constant relic abundance in the γ, δ plain serve to identify the limits. Recall that Eq. 6.7 and Fig. 6.1 were constructed under the assumption that $\Omega h^2 = 0.1$ for *all* γ', δ'. Selecting a particular pair of values (m_X, g_{XXY}) then produces a unique curve of $\Omega h^2 = 0.1$ in the γ', δ' plane. The intersection of the curve with the region where large boost factors are possible determines the consistency between relic abundance and indirect detection constraints. The critical value of m_X, g_{XXY} for which the relic curve barely enters the large boost factor region of γ', δ' then serves as an upper limit on the mass of dark matter or lower limit on the coupling strength.

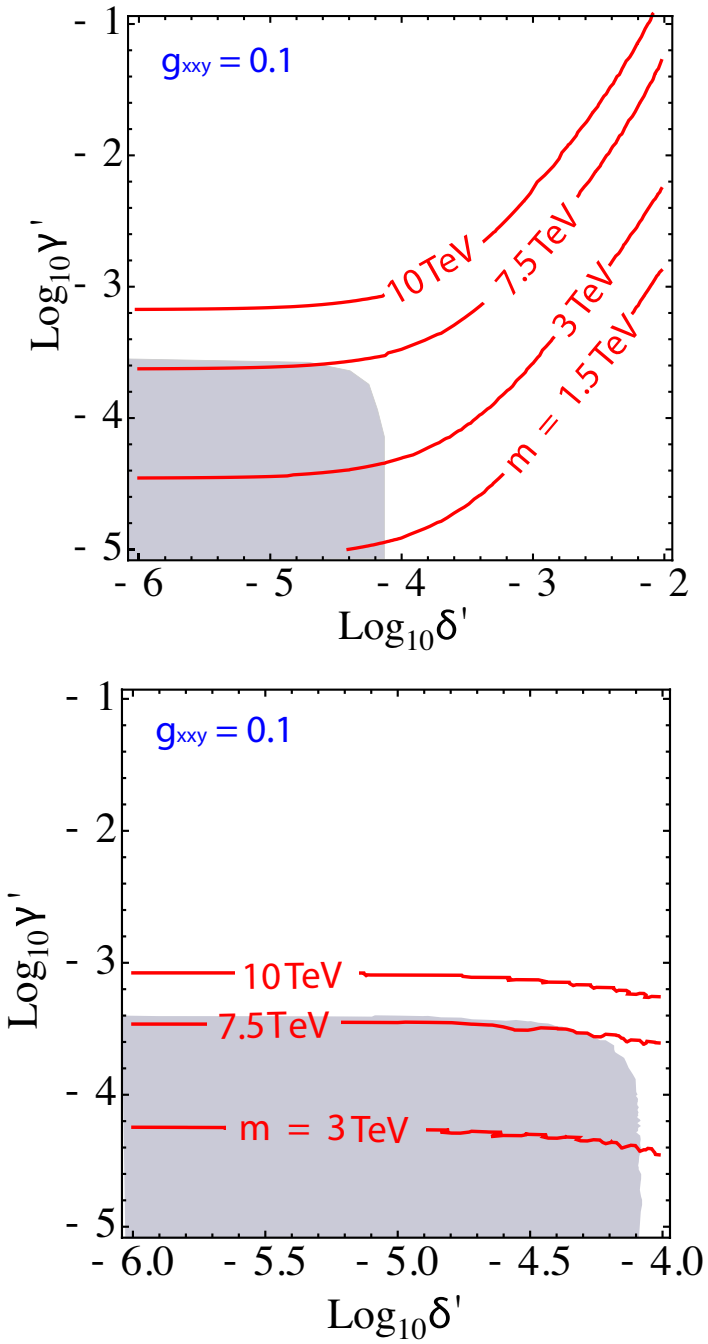

Figure 6.2: Limits on dark matter mass requiring a boost factor $BF \geq 100$ with $g_{XXY} = 0.1$. The grey shaded regions are regions where $BF \geq 100$ is achievable. The red lines are contours of $\Omega h^2 = 0.1$ for different dark matter masses. Top panel is for the pole below threshold. Bottom panel is for a pole above threshold. Smaller couplings push the red contours up. Fermionic dark matter coupling a vector resonance was used for the purpose of the graphic.

Fig. 6.2 shows the results for fermionic dark matter with a coupling $g_{XXY} = 0.1$ to a vector resonance. Solid lines represent contours of $\Omega h^2 = 0.1$ for different masses of dark matter. The gray shaded region is where $BF \geq 100$ is possible. Larger masses push the contours up into the region with no overlap between the desired $BF \geq 100$ region and $\Omega h^2 = 0.1$. The combined information thus produces a new upper limit on the dark matter mass of $m_X \approx 8TeV$, for a coupling $g_{XXY} = 0.1$. Dependence on the coupling strength is inverse of the dependence on mass. The scaling rule of 6.5 tells us that larger couplings push the contours of correct relic abundance down into the desired region of boost-factors, making heavier dark matter masses accessible. In other words, for dark matter mass of $8TeV$ the minimal coupling which allows for a $BF \sim O(100)$ is $g_{XXY} = 0.1$.

From Fig. 6.2, we can obtain an analytic approximation for the relationship between the upper limit on the mass and the lower limit on the coupling to be

$$\frac{4\pi g_{min}^2}{m_{max}^2} = \frac{4\pi\,(0.1)^2}{(7.5TeV)^2} \approx 10^{-9} GeV^{-2}. \tag{6.9}$$

Eq. 6.9 has the familiar form of the Born level estimate of the velocity averaged cross section required to obtain the correct relic abundance. In this case it serves an entirely new purpose as a relation between the *upper* and *lower* limits on relevant parameters, given a boost factor of $O(100)$. For instance, a dark matter with mass $m_X = 1TeV$ has to have a minimal coupling to the resonance of $g_{XXY} \approx 0.0025$ in order to both achieve the boost factor of $O(100)$ and the correct relic abundance.

Larger boost factors will inevitably change Eq. 6.9. While our illustration deals only with $BF = 100$, the same procedure can be used for any desired boost factor. In general, the right side of Eq. 6.9 will be a function $f \equiv f(BF_{min})$, while at this point it is not clear what this function should look like. For an answer, we turn to the region of

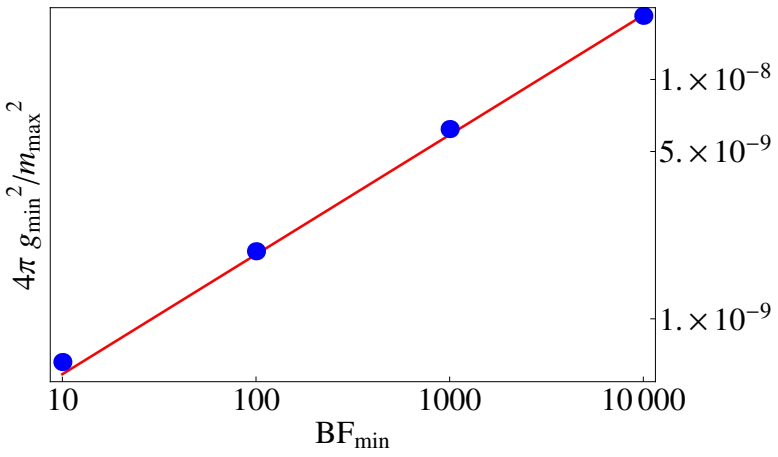

Figure 6.3: Scaling of the factor $4\pi g^2_{min}/m^2_{max}$ as a function of the minimal desired boost factor. Blue dots are different values of the factor $4\pi g^2_{min}/m^2_{max}$ given a desired boost factor. The red line is a fit of the form $a\sqrt{BF_{min}}$.

$\delta' \to 0$, which essentially defines the limiting ratio between g_{XXY} and m_X. Consider for instance the top panel of Fig. 6.2. The slope of the $\Omega h^2 = 0.1$ lines in the region $\delta' \to 0$ is essentially 0, while for larger δ' it is positive. The slope of the $\Omega h^2 = 0.1$ lines in the small δ' region is also nearly 0, while for larger δ' it becomes sharply negative. Thus, the condition of intersection between the $\Omega h^2 = 0.1$ lines and the boost factor contours is purely determined by the region $\delta' \to 0$.

Focusing on this region, we perform a numerical fit to g^2_{min}/m_{max^2} for a set of different boost factor in the region of $BF = 10 - 10^4$. Fig. 6.3 shows the result. Blue dots represent the numerical estimates of the factor $4\pi g^2_{min}/m^2_{max}$ for a set of given desired boost factors. Fit to the numerical estimates of $4\pi g^2_{min}/m^2_{max}$ using different values of BF shows a clear scaling as $f(BF) \sim \sqrt{BF}$ in the region $BF = 10 - 10^4$. The solid red line is the fit $f(BF) = 1.86 \times 10^{-10} GeV^{-2}\sqrt{BF_{min}}$.

Scaling the boost factor out of 6.9 then gives a more general formula:

$$\frac{4\pi g^2_{min}}{m^2_{max}} \approx \sqrt{BF_{min}}\ 10^{-10} GeV^{-2}. \tag{6.10}$$

Eq. 6.10 is not valid over the whole range of parameter set, but is a very good approximation in the region of $BF = 10 - 10^4$. Recall that this is the region of boost factors needed to explain the PAMELA positron excess. Eq. 6.10 allows for a variety of different models of resonant dark matter annihilation to be tested for consistency between relic density and indirect detection constraints in a remarkably simple way. Note however that specifics of initial/intermediate spins, etc. still have to be taken into account on a model to model basis and could in principle change the form of Eq. 6.10.

Conclusions

The dynamical effects of resonant processes and finite particle widths might play an important role in dark matter evolution in the early universe. Recognizing that there are many types of resonant dark matter annihilation revises the problem of relic abundance. Organizing the calculation in terms of observable quantities gives new relations between the masses and widths of intermediate states that will be consistent with fixed relic abundance.

Given that particle widths are generally calculable, our mass-v-width relations develop into mass-v-mass consistency relations between the dark matter with a given relic density and the mass of an s-channel connector. Depending on the model, this produces a significant revision of a traditional rule $\langle \sigma v \rangle_0 \sim 3 \times 10^{-26} cm^3/s$. The relation between m_X and m_Y depends on the way the width is calculated, but in a broad class of models permits an unlimited range of both masses. Our relations can be used to test candidates for dark matter, while also eliminating much of the need to re-compute relic evolution on a model-by-model basis.

Furthermore, we have explored significant effects in halo annihilation rates due to natural widths of intermediate states. The problem is intricate due to subtle interplay of energy scales. Tiny values of galactic halo velocities reverse an assumption that propagator widths might be "small corrections." Given that TeV-scale particles with typical electro-weak couplings may easily have $\Gamma/E_0 >> 1$, Breit-Wigner factors of

ordinary radiative corrections must generally be taken into account. Consistency of rates in particular channels, such as the apparent dominance of leptons, still needs to be considered model by model. We find exotic "Sommerfeld factors" to have no strong foundation in particle theory. Approximations made to produce large enhancements at low velocity typically break down in the regions where the enhancement is much greater than $O(1)$.

Combining relic density and halo constraints produced further limits. Past analyses of resonant dark matter annihilation typically focused on a subset of the complete parameter set, overlooking the intricate relationships between the masses, widths and couplings in the problem. Taking into account the full parameter set allowed us to use combined constraints to develop new limits on dark matter mass and couplings. Our result revises the standard $\langle \sigma v \rangle_0 = 4\pi g^2/m_x^2 \sim 10^{-9} GeV^{-2}$ from an estimate of the annihilation rate to the useful limit on the mass of dark matter and the couplings.

Appendices

A.1 Derivation of the Boltzmann Equation

The form of the Boltzmann equation in Eq. 3.7

$$\frac{dY}{dx} = -\frac{xs(x)\langle\sigma v\rangle}{H(m)}(Y^2 - Y_{EQ}^2), \tag{A.1}$$

is commonly found in dark matter literature. However, it is very rare that authors discuss the assumptions made during derivation. In this appendix, we present a full derivation of Eq. 3.7 and clarify all the necessary assumptions, following the conventions and notation of Ref. [41].

To begin, let us first look at the general form of the non-relativistic Boltzmann equation. A statement of conservation of phase space volume, the Boltzmann equation for a collision-less system can be written in the form

$$\frac{df}{dt} = \left(\frac{\partial}{\partial t} + \frac{\partial \vec{x}}{\partial t}\frac{\partial}{\partial \vec{x}} + \frac{\partial \vec{p}}{\partial t}\frac{\partial}{\partial \vec{p}}\right) f = 0, \tag{A.2}$$

where

$$f \equiv f(\vec{x}, \vec{p}, t) \tag{A.3}$$

is a phase space distribution.

The equivalent equation in curved space-time takes the form

$$\left(p^\mu \frac{\partial}{\partial x^\mu} - \Gamma^\mu_{\nu\alpha}\, p^\nu p^\alpha \frac{\partial}{\partial p^\mu}\right) f = 0. \tag{A.4}$$

Here $\Gamma^\mu_{\nu\alpha}$ is the Christoffel symbol

$$\Gamma^\mu_{\nu\alpha} = \frac{1}{2} g^{\mu\lambda}\left(\partial_\alpha g_{\lambda\nu} + \partial_\nu g_{\lambda\alpha} - \partial_\lambda g_{\nu\alpha}\right). \tag{A.5}$$

In the presence of interactions, the right side of Eq. A.4 is non-zero. For illustration we will only consider $2 \to 2$ interactions.

Adding an interaction term, Eq. A.4 becomes

$$\left(p^{\mu} \frac{\partial}{\partial x^{\mu}} - \Gamma^{\mu}_{\nu\alpha} p^{\nu} p^{\alpha} \frac{\partial}{\partial p^{\mu}} \right) f = \frac{\partial f}{\partial t}_{col}. \tag{A.6}$$

We first look at the left side of the equation Eq. A.6. Assuming the Robertson-Walker (RW) metric, which is spatially isotropic and homogeneous, allows us to eliminate all spatial derivatives. Furthermore, taking into account that $\Gamma^0_{ij} = \dot{R}/R\, g_{ij}$ where R is the scale factor from the RW metric, we get

$$E \frac{\partial f(E,t)}{\partial t} - \Gamma^0_{ij} p_i p_j \frac{\partial f}{\partial E} \;\; = \;\; E \frac{\partial f}{\partial t} - \frac{\dot{R}}{R} |\vec{p}|^2 \frac{\partial f}{\partial E} = \frac{\partial f}{\partial t}_{col}. \tag{A.7}$$

Ultimately, we are interested in number density of particles

$$n(t) = dN/dV = \frac{1}{(2\pi)^3} \int d^3p\, f(E,t). \tag{A.8}$$

Integrating Eq. A.8 by parts gives

$$n(t) = -\frac{1}{(2\pi)^3} \int d^3p \frac{1}{3} |\vec{p}| \frac{\partial f(E,t)}{\partial |\vec{p}|} = -\frac{1}{(2\pi)^3} \int d^3p \frac{1}{3} \frac{|\vec{p}|^2}{E} \frac{\partial f(E,t)}{\partial E}. \tag{A.9}$$

Integrating Eq. A.7 and using Eqs. A.8 and A.9, we can now rewrite the Boltzmann equation as

$$\frac{\partial n}{\partial t} + 3Hn = -\frac{1}{(2\pi)^3} \int \frac{\mathrm{d}^3 p}{E} \frac{\partial f}{\partial t}_{col}. \tag{A.10}$$

In the last step we've introduced the Hubble parameter $H \equiv \dot{R}/R$.

It is common and useful to introduce a dimensionless variable

$$Y \equiv \frac{n}{s}, \tag{A.11}$$

where s is the entropy density. We assume the universe is expanding adiabatically. Then by conservation of entropy in the co-moving volume, $sR^3 = const$ and so

$$\frac{\partial Y}{\partial t} = \frac{1}{s}(\dot{n} + 3Hn) = \frac{1}{s}\frac{1}{(2\pi)^3}\int \frac{\mathrm{d}^3 p}{E}\frac{\partial f}{\partial t}_{col}. \tag{A.12}$$

In standard cosmology the time and temperature T are related by

$$t = \frac{0.301}{\sqrt{g_*}}\frac{m_{PL}}{T^2}, \tag{A.13}$$

where g_* is the number of relativistic degrees of freedom and m_{PL} is the Planck mass. Introducing x=m/T, and transferring the time derivative in Eq. A.12 to x then gives

$$\frac{dY}{dx} = -\frac{x}{H(m)\,s} \times \frac{1}{(2\pi)^3}\int \frac{\mathrm{d}^3 p}{E}\frac{\partial f}{\partial t}_{col}. \tag{A.14}$$

Here $H(m) = 1.67 g_*^{1/2} m^2/m_{PL}$. The integral on the right side of Eq. A.14 represents the rate at which the number density is changing. In general, for a $2 \to 2$ process, the interaction term can be written as

$$\begin{aligned}\frac{\partial f}{\partial t}_{col} &= \frac{G}{(2\pi)^{12}}\int \prod_{i=b,c,d}\frac{d^3 p_i}{2E_i}(2\pi)^4\delta^4(p_a + p_b - p_c - p_d) \\ &\quad \times \left(|M_{ab\to cd}|^2 F(p_a, p_b, t) - |M_{cd\to ab}|^2 F(p_c, p_d, t)\right),\end{aligned} \tag{A.15}$$

where $G = \prod_i g_i$ is the factor stemming from internal degrees of freedom of particles involved and F is the two particle phase space distribution of the initial/final state.

Depending on the density of the interacting gas, the strength and form of the interaction, F can in principle have almost any form of a reasonable probability distribution with any level of correlation between the two initial state particles. To proceed, we make an important assumption that the initial state particles are *uncorrelated*. In statistical mechanics, this is usually referred to as Boltzmann's assumption of "Molecular Chaos," and is justified by either weak interaction strength between the particles or low density.

The assumption of uncorrelated distributions expresses F as

$$F(p_a, p_b) = f_a f_b \quad and \quad F(p_c, p_d) = f_c f_d. \tag{A.16}$$

Next, we make an assumption that the process we consider is even under time reversal. In other words

$$|M_{ab\to cd}|^2 = |M_{cd\to ab}|^2. \tag{A.17}$$

By the CPT theorem, the process is then also CP even. Eq. A.15 can be generalized to processes which are CP violating by keeping track of the individual $ab \to cd$ and $cd \to ba$ amplitudes.

With these assumptions, we can simplify the form of Eq. A.15 to

$$\begin{aligned} \frac{\partial f}{\partial t}_{col} &= \frac{G}{(2\pi)^9} \int \prod_{i=b,c,d} \frac{d^3 p_i}{2E_i} (2\pi)^4 \delta^4 (p_a + p_b - p_c - p_d) \\ &\quad \times |M_{ab\to cd}|^2 \left(f_c f_d - f_a f_b\right). \end{aligned} \tag{A.18}$$

To continue, we assume that all final state particles have the ability to interact through forces much stronger than the interaction with dark matter, forcing them into thermal equilibrium. The distribution of final state particles then takes the form

$$f_{c,d} = e^{-E_{c,d}/T}. \tag{A.19}$$

By conservation of energy, we can replace the term $f_c f_d$ in Eq. A.18 with

$$f_c f_d \to f_a^{EQ} f_b^{EQ}. \tag{A.20}$$

Next, we need to integrate Eq. A.18 to get an expression in terms of number density $n(t)$:

$$\begin{aligned}
\frac{\partial n}{\partial t}_{col} &= \frac{1}{(2\pi)^3}\int \frac{d^3p_a}{E_a}\frac{\partial f}{\partial t}_{col} \\
&= \frac{1}{(2\pi)^{12}}\int \prod_{i=a,b,c,d}\frac{d^3p_i}{2E_i}(2\pi)^4\delta^4(p_a+p_b-p_c-p_d) \\
&\quad \times|M_{ab\to cd}|^2\left(f_a f_b - f_a^{EQ} f_b^{EQ}\right).
\end{aligned} \tag{A.21}$$

In the first step of Eq. A.21 we attached an index a to the integration variable to clarify the momentum which should be integrated. The same holds for the left side of the Boltzmann equation we derived earlier. Neglecting the spin effects of Bose-Einstein vs. Fermi statistics, we assume a simple Maxwell-Boltzmann type distribution. This approximation is valid for non-relativistic species. Assuming classical, spin-less distributions allows us to write

$$f_{a,b} = e^{\mu/T} f_{a,b}^{EQ}, \tag{A.22}$$

where μ is the chemical potential, assumed to be a slowly varying function of $\vec{p}$.

Plugging Eq. A.22 into Eq. A.21 turns the integral into

$$\begin{aligned}
\frac{\partial n}{\partial t}_{col} &= \frac{1}{(2\pi)^{12}}\left(e^{2\mu/T}-1\right)\frac{n_{EQ}^2}{n_{EQ}^2} \\
&\quad \times\int \prod_{i=a,b,c,d}\frac{d^3p_i}{2E_i}(2\pi)^4\delta^4(p_a+p_b-p_c-p_d) \\
&\quad \times|M_{ab\to cd}|^2 f_a^{EQ} f_b^{EQ}.
\end{aligned} \tag{A.23}$$

Note that by definition, the thermally averaged cross section is

$$\langle \sigma v \rangle \equiv \frac{1}{(2\pi)^{12}} \frac{1}{n_{EQ}^2} \int \prod_{i=a,b,c,d} \frac{d^3 p_i}{2E_i} (2\pi)^4 \delta^4 (p_a + p_b - p_c - p_d) |M_{ab\to cd}|^2 f_a^{EQ} f_b^{EQ}. \tag{A.24}$$

Here we only considered a two particle final state. Notice that adding more annihilation channels will simply modify $\langle \sigma v \rangle$. The rest of the derivation is unaffected. Substituting the definition of $\langle \sigma v \rangle$ into Eq. A.23 then gives

$$\frac{\partial n}{\partial t}_{col} = \langle \sigma v \rangle (n^2 - n_{EQ}^2). \tag{A.25}$$

Finally, substituting Eq. A.25 into the right side of Eq. A.10 gives us the usual form of the Boltzmann equation

$$\frac{\partial n}{\partial t} + 3Hn = -\langle \sigma v \rangle (n^2 - n_{EQ}^2). \tag{A.26}$$

From here, using the definition of $Y \equiv n/s$ it is trivial to transform the equation into the desired form:

$$\frac{dY}{dx} = -\frac{xs(x)\langle \sigma v \rangle}{H(m)} (Y^2 - Y_{EQ}^2). \tag{A.27}$$

To summarize, we obtained a widely cited rate equation in Eq. 3.7 starting from a general form of the Boltzmann equation in curved space-time. It is important to note that during the derivation we made the following assumptions:

1. There is only one species of dark matter.

2. The phase space distribution of the initial state particles in uncorrelated: $F(p_a, p_b) = f_a f_b$.

3. The process is even under T and CP: $|M_{if}|^2 = |M_{fi}|^2$.

4. The metric is of a Robertson-Walker form: $f \neq f(\vec{x})$.

5. The universe is expanding adiabatically: $sR^3 = const$.

6. All final state species are in thermal equilibrium: $f \sim e^{-E/T}$.

7. The only species going out of equilibrium is the dark matter species.

8. There is no particle-antiparticle number asymmetry: $f_X = f_{\overline{X}}$.

9. Effects of quantum degeneracy are negligible: $f_X = e^{\mu/T} f_{EQ}$, $\mu \neq \mu(\vec{p})$.

A separate treatment of the Boltzmann equation is required whenever any of the above assumptions is violated. For instance, introducing more dark matter species will in general require a system of coupled differential equations. A strongly interacting or overly dense dark matter gas will violate assumption of uncorrelated initial state particle distributions. Furthermore, CP odd processes require a careful and separate treatment of $|M_{i\to f}|^2$ and $|M_{f\to i}|^2$. If dark matter annihilates into species that are weakly interacting, it becomes questionable to assume that all final state species are in thermal equilibrium.

A.2 Relic Abundance Code

To calculate relic abundance we have in part used MadDM v0.1 code [37]. MadDM is a python package designed as an extension of MadGraph [38] for the purpose of dark matter physics. MadDM is an ongoing project, with a scope and timeline beyond the work in this thesis. The use of the MadDM v0.1 code here was primarily intended as a proof of principle that the code can accurately incorporate resonant poles into the relic abundance calculations. The original code was modified to accommodate resonant annihilation cross sections, which are currently not an intrinsic part of MadDM v0.1.

MadDM is envisioned to heavily rely on the existing MadGraph architecture for diagram and matrix element generation. The general algorithm of the MadDM code can be summarized in the following steps

1. Load MadGraph model
2. Find the dark matter candidates by looking for the stable, electrically neutral, colorless particles in the model.
3. Generate annihilation diagrams to standard model particles and the corresponding matrix elements.
4. Calculate the annihilation cross section and the corresponding $\langle \sigma v \rangle(x)$.
5. Solve the Boltzmann Equation to obtain Ωh^2.

A.2.1 Main Program

The following is the main program used to calculate dark matter relic abundance. The code is designed to perform a sequential parameter scan over a two dimensional parameter space of resonant widths and masses. The couplings, mass of dark matter as well as the initial and intermediate state spins are inputs of the code. Generalizations of the code to scan over any number of parameters is trivial.

```
from darkmatter import *

coupling= 0.1
DMmass = 300.0
cjj = 1.0

dm = darkmatter()

dm.gxxy = coupling
```

```
dm.mDM.append([DMmass, DMmass])
dm.gDM.append([3.0,3.0])

steps = [1.0+ 0.5*x for x in range(0, 18)]
steps2 = [1.0+ 0.5*x for x in range(0, 18)]
steps3 = [1.0+ 0.5*x for x in range(0, 18)]
steps4 = [1.0+ 0.5*x for x in range(0, 18)]

deltas = [10.0**(-6)*i for i in steps]+\
        [10.0**(-5)*i for i in steps2]+\
        [10.0**(-4)*i for i in steps3]+\
        [10.0**(-3)*i for i in steps4]

gammas = [10.0**(-5)*i for i in steps]+\
        [10.0**(-4)*i for i in steps2]+\
        [10.0**(-3)*i for i in steps3]+\
        [10.0**(-2)*i for i in steps4]

widths = [gamma*DMmass for gamma in gammas]
ymasses = [2.0*DMmass*(1.0 - delta) for delta in deltas]


for Ymass in ymasses:

    for GammaY in widths:

        dm.Gy = GammaY
        dm.My = Ymass
        dm.tjj = cjj*dm.My**2 #tjj is now Cjj

        dm.init_sigv()

        omega = dm.relicdensity\
         (0.1, 10000, 1, 51.0, 15.0, 50, 0.1)[2]

        print str(dm.My) \
           +" "+str(dm.Gy) \
           +" "+str(omega)
```

A.2.2 MadDM darkmatter class

This section contains the code of the darkmatter class used in the main code. We only present the parts of code relevant for the calculations in this thesis, as the entire code is too long. The darkmatter class is a part of the MadDM v0.1 package. The

structure of the class consists of a darkmatter object which contains all the relevant information needed to calculate relic abundance as well as methods which perform the relic abundance calculation. There are only two relevant methods used directly in our main program: **init_sigv** which initializes calculates and sets up the velocity averaged cross section for a given parameter set, and **relicdensity** which calculates the relic density and other parameters in the form $(x_f, Y_\infty, \Omega h^2, g_*(x_f))$. For examples of how to use the class and the associated methods look at the main code in Section A.2.1

```
from phasespace import *
from nr import *
from math import pi
from math import exp
from math import atan
from math import sqrt

#Conversion factor for the cross section. WRONG!
pbtogev = 0.3894/(10.0**9)


class darkmatter:

    #initializion of a DM object.
    def __init__(self):

        #Read in array of g_* from a file
        try:
            inputfile = open('g_star.txt', 'r')
            inputfile.seek(0)
            data = inputfile.readlines()

            inputfile.close()

        except OSError:
            print "Could not find or open g_star.txt!"
            exit

        gx = []; gy = []
        # store data pairs in lists x and y
        for line in data:
            xval, yval = line.split()
            gx.append(float(xval))
            gy.append(float(yval))
```

```
        #Initialize the object elements
        self.paramcard = 'NONE'
        self.gDM = []
        self.mDM = []
        self.pdgID = []
        self.mpl = 1.2209*(10.0**(19))
        self.g_star_x = gx
        self.g_star_y = gy
        self.modelname = 'NONE'
        self.Wij = ['NONE','NONE'] #Matrix of cross sections
        self.SigmaV = ['NONE','NONE']
        #where each element has the form [[s], [sigma]]

        self.gxxy = 0
        self.Gy = 0
        self.My = 0
        self.sigvtoday = 0
        self.tjj = 0
        self.gamma = 0
        self.delta = 0

        #Needed for numerical calculations
        self._x = 1.0

        #miscelaneous MadGraph object elements
        self.full_model = None
        self.Model = None
        self.helas_writer = None
        self.helas_multi_proc = None
        self.stored_quantities = {}
        self.matrixelements = None



#-------------------------------------------------
#                       METHODS:
#-------------------------------------------------

    def init_sigv(self):

    #Calculate Wij

            #THIS SHOULD BE SUPPLIED BY THE USER!!!!!!!
            steps = 10000

            srange = []
            for j in range(1, steps):
                beta = 1-exp(-float(j) / float(steps))
                srange.append(float(4*self.mDM[0][0]*self.mDM[0][0] \
```

```
     / (1 - beta*beta)))

sigma = []

for s in srange:
    #print "!!!!!!"

    bf = 1.0

    vcm = sqrt(1 - 4.0*self.mDM[0][0]**2 / s)

    #!!!!!!!!!!!!!!!!!!!!!!!!!!!!
    #HERE IS THE CROSS SECTION
    #!!!!!!!!!!!!!!!!!!!!!!!!!!!!
    wij =  bf*self.gxxy**2/(4.0*self.mDM[0][0]**2 * vcm)\
         *(self.tjj*self.My*self.Gy) \
        /((s - self.My**2)**2 + (self.My*self.Gy)**2) \
        *2.0*s*vcm #to convert sig to wij

    #romberg_mod(self.ResonanceME, s)
    sig = 1.0/(2.0*sqrt(s**2-4*self.mDM[0][0]**2*s))\
     *3.89391e8*wij

    # Call to return numerical value of the matrix element
    #at cos(theta) = 0
    # self.MatrixElement(1.0, s)

    sigma.append(wij)


#SET UP Wij elements of the dark matter object
self.Wij[0] = srange
self.Wij[1] = sigma

xsteps = 200
#Calculate and set sigmav
x_range = []
for j in range(1, xsteps):
    x_range.append(1.0+1.0*j)

#print "Now calculating sigmav..."
sigv = []
t0prim = time.time()
for xprim in x_range:
    self._x = xprim
    sigv.append(romberg_mod(self.taacs, xprim))
t1prim = time.time()

#print "---Finished calculating sigmav in "+\
 str(t1prim - t0prim)+" seconds."
self.SigmaV[0] = x_range
```

```
            self.SigmaV[1]= sigv

            self.sigvtoday = romberg_mod(self.taacs, 1.0e6)

    #-------------------------------------------------------
    # Thermally Averaged Annihilation Cross Section (sigma*v)
    #-------------------------------------------------------
    def sigmav(self):
        return lineint(float(self._x), self.SigmaV[0],\
          self.SigmaV[1])
        #return romberg(self.taacs)
        #return 2.3*10.0**(-9)


    #--------------------------------------
    # Interpolating points for getWij
    #--------------------------------------
    def getWij(self,svalue):
        #print cubeint(float(svalue),self.Wij[0],self.Wij[1])
        return lineint(float(svalue),self.Wij[0],self.Wij[1])

-----------------------------------------------
# integrand for sigma*v
#-----------------------------------------------
    def taacs(self, beta, xx):
        coeff = (xx)**(3.0/2.0)/(self.mDM[0][0]**2*(pi)**(0.5))
        s = 4.0*self.mDM[0][0]**2/(1.0-beta**2)
        Wij_value = self.getWij(s)
        middle = beta**2/(1.0-beta**2)**(2.25)*exp(-2.0*(xx)*\
            (1.0/(1.0-beta**2)**(0.5)-1.0))

        return coeff*middle*Wij_value

    #-------------------------------------------------------
    # Interpolate points for getgstar(T)
    # WARNING: This function is in terms of temperature!
    #-------------------------------------------------------
    def getgstar(self,temp):
        return cubeint(temp,self.g_star_x,self.g_star_y)

    def Yeq(self):
        if self._x > 100.0:
            return 10**-30

        return 45/(4.0*pi**4)*(pi/2.0)**0.5*self.gDM[0][0]/self.\
            getgstar(self.mDM[0][0]/self._x)*\
            (self._x)**(1.5)*exp(-self._x)

    def H(self):
        return (4*pi**3.0 / 45.0)**0.5*\
           self.getgstar(self.mDM[0][0]/self._x)**0.5*\
```

```
        self.mDM[0][0]**2.0/self.mpl

def s(self):
    return 2*pi**2/45*self.getgstar(self.mDM[0][0]/self._x)*\
        (self.mDM[0][0]/self._x)**3

#-----------------------------
#Define the Boltzman equation
#-----------------------------
def dydx(self, x, y):
    self._x = x
    #print (y[0]**2.0-self.Yeq()**2.0)
    #print "{"+str(self._x)+","+str(self.sigmav())+"},"
    return [-1*self._x*self.sigmav()*self.s()/self.H()*\
        (y[0]**2.0-self.Yeq()**2.0)]


#-----------------------------------------------------
#Calculates Omega at infinity. Returns an array [xf, Yf],
#where xf is the freezeout
#defined by the condition |Y - Yeq| > 1/2 Yeq
#Yprecission = Yf[i] - yYf[i-1])/Yf[i]
#xfin - where to stop integration
#x0max, x0min, Nx0 - creates an array of x values from
# which to start the
#         integration. array starts at x0max goes to x0min
#         and has Nx0 values in between
#xfprec - precision in estimation of xf
#x0min, x0max MUST BE IN FLOAT FORMAT!
#-----------------------------------------------
def relicdensity\
 (self,Yprecission, xfin, dx0, x0max, x0min, Nx0, xfprec):

    #Check if cross section is calculated before
    #calculating Omega.
    if self.Wij == []:
        print "Matrix element has not been calculated yet!"
        exit

    #Set up initial conditions and params for ode solver.
    #WARNING: y0 must be in an array! y must always be
    #indexed as an array!
    nvar = 1
    #x values to start integration from
    xstart= [float(x0max) - (float(x0max)-float(x0min))\
        /float(Nx0)*k\
        for k in range(Nx0)]
    yfs=[]

    #Solve the Boltzman Equation.
    #yf -final value of Y
```

```
#yp - intermediate values of Y
#xp - intermediate values of x
#kount - how many intermediate points in xp, yp

i=0
for x0 in xstart:
    self._x = x0
    y0 = [self.Yeq()]
    [yf,nok,nbad, kount, xp, yp] = odeint(y0, nvar, \
        float(x0),float(xfin), float(dx0), self.dydx, \
            eps = 1e-2, hmin = 1e-60,\
            kmax = 10000, dxsav=xfprec)
    yfs.append(yf[0])

    if ((i > 0.0) & (abs(yfs[i] - yfs[i-1])/yfs[i] \
             < Yprecission)) :
        break
    i=i+1


#Calculate the freezeout time
j = 0
xf = 1.0
#xp[j] - removed from Yeq

#print yp[0][j], self.Yeq(), yp[0][j] - self.Yeq()
self._x = xp[0]
while (abs(yp[0][j] - self.Yeq()) < 0.5*self.Yeq()):
    #print xp[j], yp[0][j], self.Yeq()
    xf = xp[j]
    j=j+1
    self._x = xp[j]

OmegaDM = yf[0]*self.mDM[0][0]*2889.2/(1.05*10**(-5.0))

#array to return
results = [xf, yf[0], OmegaDM, \
              self.getgstar(self.mDM[0][0]/xf)]

return results
```

A.2.3 Numerical Recipees code

This section contains the code for the numerical recipees used in the darkmatter class.

The functions defined in this code can be grouped as follows:

- **Interpolating functions (cubeint, lineint)** - Used to interpolate numerically evaluated functions.
- **ODE solvers (odeint)** - A Runge Kutta ODE solver used to solve the Boltzmann equation.
- **One dimensional integrators (romberg, romberg_mod)** - Romberg method integrators.

```
from math import copysign

def getindex(xvalue,x,y):
  if (xvalue < x[0]):
    return 1
  if (xvalue > x[len(x)-1]):
    return (len(x)-2)

  lowindex = 0
  highindex = len(x)
  while ((highindex-lowindex) > 1):
    mid = (highindex+lowindex)//2
    if (x[mid] <= xvalue): lowindex = mid
    if (x[mid] > xvalue): highindex = mid
  return lowindex

def cubeint(xval,xs,ys):
  i = getindex(xval,xs,ys)
  if (i == 0):
    x = [xs[0],xs[1],xs[2],xs[3]]
    y = [ys[0],ys[1],ys[2],ys[3]]
  elif (i == len(xs)-2):
    x = [xs[len(xs)-4],xs[len(xs)-3],xs[len(xs)-2],xs[len(xs)-1]]
    y = [ys[len(xs)-4],ys[len(xs)-3],ys[len(xs)-2],ys[len(xs)-1]]
  else:
    x = [xs[i-1],xs[i],xs[i+1],xs[i+2]]
    y = [ys[i-1],ys[i],ys[i+1],ys[i+2]]
  A = y[3]/((x[3]-x[0])*(x[3]-x[1])*(x[3]-x[2]))
  B = y[2]/((x[2]-x[0])*(x[2]-x[1])*(x[2]-x[3]))
  C = y[1]/((x[1]-x[0])*(x[1]-x[2])*(x[1]-x[3]))
  D = y[0]/((x[0]-x[1])*(x[0]-x[2])*(x[0]-x[3]))
  result = A*(xval-x[0])*(xval-x[1])*(xval-x[2]) \
      +B*(xval-x[0])*(xval-x[1])*(xval-x[3]) \
      +C*(xval-x[0])*(xval-x[2])*(xval-x[3]) \
      +D*(xval-x[1])*(xval-x[2])*(xval-x[3])
```

```
  return result



def rkck(y,dydx,n,x,h,derivs):
  c = [1.0/5.0,3.0/10.0,3.0/5.0,1.0,7.0/8.0]
  a = [[1.0/5.0,0.0,0.0,0.0,0.0],\
      [3.0/40.0,9.0/40.0,0.0,0.0,0.0],\
      [3.0/10.0,-9.0/10.0,6.0/5.0,0.0,0.0],\
      [-11.0/54.0,5.0/2.0,-70.0/27.0,-35.0/27.0,0.0],\
      [1631.0/55296.0,175.0/512.0,575.0/13824.0\
      44275.0/110592.0,253.0/4096.0]]
  b = [37.0/378.0,0.0,250.0/621.0,125.0/594.0,0.0,\
      512.0/1771.0]
  b_star = [2825.0/27648.0,0.0,18575.0/48384.0\
     ,13525.0/55296.0,277.0/14336.0,1.0/4.0]
  K = [[0.0 for i in range(n)] for j in range(6)]
  ytemp = [0.0 for i in range(n)]
  yout = [0.0 for i in range(n)]
  yerr = [0.0 for i in range(n)]
  for i in range(n):
    K[0][i] = dydx[i]
  for i in range(5):
    for j in range(n):
      ytemp[j] = y[j]
      for k in range(5):
        ytemp[j] += h*a[i][k]*K[k][j]
    dydxtemp = derivs(x+h*c[i],ytemp)
    for j in range(n):
      K[i+1][j] = dydxtemp[j]
  for i in range(n):
    yout[i] = y[i]
    for j in range(6):
      yout[i] += h*b_star[j]*K[j][i]
      yerr[i] += h*(b[j]-b_star[j])*K[j][i]
  results = [yout,yerr]
  return results



def rkqs(y,dydx,n,x,htry,eps,yscal,derivs):
  [safety, pgrow, pshrink, errcon, flag] =\
         [0.9, -0.2, -0.25, 1.89e-4, 1]
  h = htry
  while True:
    [yout,yerr] = rkck(y,dydx,n,x,h,derivs)
    errmax = 0.0
    for i in range(n):
      errmax = max(errmax,abs(yerr[i]/yscal[i]))
    errmax = errmax/eps
    if errmax > 1.0:
```

```
      htemp = safety*h*(errmax**pshrink)
      h = copysign(max(abs(htemp), 0.1*abs(h)), h)
      xnew = x + h
      if (xnew  == x): print 'stepsize underflow in rkqs'
    else:
      if (errmax > errcon):
        hnext = safety*h*(errmax**pgrow)
      else:
        hnext = 5.0*h
      hdid = h
      x = x + h
      for i in range(n):
        y[i] = yout[i]
        results = [x,yout,hdid,hnext]
      return results



def odeint(ystart, nvar, x1, x2, h1, derivs, \
      eps = 1e-20, hmin = 1e-50,\
      kmax = 0, dxsav = 0.1):
  [nok, nbad, kount] = [0, 0, 0]
  xp = [0.0 for i in range(kmax)]
  yp = [[0.0 for i in range(kmax)] for j in range(nvar)]
  x = x1
  h = copysign(h1,x2-x1)
  y = [0.0 for i in range(nvar)]
  yscal = [0.0 for i in range(nvar)]
  for i in range(nvar):
    y[i] = ystart[i]
  if kmax > 0: xsav = x-2.0*dxsav
  while True:
    dydx = derivs(x,y)
    for i in range(nvar):
      yscal[i] = abs(y[i])+abs(h*dydx[i])+1e-30
    if kmax > 0:
      if (abs(x-xsav) > abs(dxsav)):
        if(kount < kmax-1):
          xp[kount] = x
          for i in range(nvar):
            yp[i][kount] = y[i]
          xsav = x
          kount += 1
    if ((x+h-x2)*(x+h-x1) > 0.0): h = x2 - x
    [x,y,hdid,hnext] = rkqs(y,dydx,nvar,x,h\
           ,eps,yscal,derivs)
    if hdid == h:
      nok += 1
    else:
      nbad += 1
    if (x-x2)*(x2-x1) >= 0.0:
```

```
      if kmax != 0:
        xp[kount] = x
        for i in range(nvar):
          yp[i][kount] = y[i]
        kount += 1
        results = [y,nok,nbad,kount,xp,yp]
        return results
      results = [y,nok,nbad]
      return results
    if (abs(hnext) < hmin): print 'stepsize \
              smaller than minimum in odeint'
    h = hnext

def lineint(xval,x,y):
index = getindex(xval,x,y)
return y[index] + (y[index+1]-y[index])\
    /(x[index+1]-x[index])*(xval-x[index])

def romberg(f, eps = 1e-3):
  R = [[0.5*(f(0.0)+f(0.99999))]]
  n = 1
  while True:
    h = 0.99999/2.0**n
    R.append((n+1)*[None])
    R[n][0] = 0.5*R[n-1][0] + h*sum(f((2*k-1)*h) \
            for k in range(1,2**(n-1)+1))
    for m in range(1,n+1):
      R[n][m] = R[n][m-1] + (R[n][m-1] - \
                R[n-1][m-1]) / (4**m - 1)
    if abs(R[n][n-1] - R[n][n]) < eps:
      return R[n][n]
    n += 1

def print_row(lst):
      print ' '.join('%11.8f' % x for x in lst)

def romberg_mod(f, var, eps = 1E-3):

  R = [[0.5*(f(0.0,var)+f(0.9999999999,var))]]
  n = 1
#  print 'NEW INTEGRATION'
  while True:
#    h = 1.0/2.0**n
    h = 0.99999/2.0**n
    R.append((n+1)*[None])
    R[n][0] = 0.5*R[n-1][0] + h*sum(f((2*k-1)*h,var)\
           for k in range(1,2**(n-1)+1))
    for m in range(1,n+1):
      R[n][m] = R[n][m-1] + (R[n][m-1] - \
                  R[n-1][m-1]) / (4**m - 1)
#    print_row(R[n])
```

```
if abs(R[n][n-1] - R[n][n])/(R[n][n] + 1.0e-50)\
       < eps:
  return R[n][n]
n += 1
```

Bibliography

[1] F. Zwicky. Die Rotverschiebung von extragalaktischen Nebeln. *Helvetica Physica Acta*, 6:110–127, 1933.

[2] Vera C. Rubin and Jr. Ford, W.Kent. Rotation of the Andromeda Nebula from a Spectroscopic Survey of Emission Regions. *Astrophys.J.*, 159:379–403, 1970.

[3] V.C. Rubin, N. Thonnard, and Jr. Ford, W.K. Rotational properties of 21 SC galaxies with a large range of luminosities and radii, from NGC 4605 /R = 4kpc/ to UGC 2885 /R = 122 kpc/. *Astrophys.J.*, 238:471, 1980.

[4] N. Jarosik et al. Seven-Year Wilkinson Microwave Anisotropy Probe (WMAP) Observations: Sky Maps, Systematic Errors, and Basic Results. *Astrophys. J. Suppl.*, 192:14, 2011.

[5] Z. Ahmed, D. S. Akerib, S. Arrenberg, C. N. Bailey, D. Balakishiyeva, L. Baudis, D. A. Bauer, P. L. Brink, T. Bruch, R. Bunker, B. Cabrera, D. O. Caldwell, J. Cooley, E. do Couto e Silva, P. Cushman, M. Daal, F. DeJongh, P. Di Stefano, M. R. Dragowsky, L. Duong, S. Fallows, E. Figueroa-Feliciano, J. Filippini, J. Fox, M. Fritts, S. R. Golwala, J. Hall, R. Hennings-Yeomans, S. A. Hertel, D. Holmgren, L. Hsu, M. E. Huber, O. Kamaev, M. Kiveni, M. Kos, S. W. Leman, S. Liu, R. Mahapatra, V. Mandic, K. A. McCarthy, N. Mirabolfathi, D. Moore, H. Nelson, R. W. Ogburn, A. Phipps, M. Pyle, X. Qiu, E. Ramberg, W. Rau, A. Reisetter,

R. Resch, T. Saab, B. Sadoulet, J. Sander, R. W. Schnee, D. N. Seitz, B. Serfass, K. M. Sundqvist, M. Tarka, P. Wikus, S. Yellin, J. Yoo, B. A. Young, and J. Zhang. Results from a low-energy analysis of the cdms ii germanium data. *Phys. Rev. Lett.*, 106(13):131302, Mar 2011.

[6] R. Bernabei et al. Particle Dark Matter and DAMA/LIBRA. *AIP Conf. Proc.*, 1223:50–59, 2010.

[7] C. E. Aalseth et al. Results from a Search for Light-Mass Dark Matter with a P-type Point Contact Germanium Detector. *Phys. Rev. Lett.*, 106:131301, 2011.

[8] E. Aprile and T. Doke. Liquid xenon detectors for particle physics and astrophysics. *Rev. Mod. Phys.*, 82(3):2053–2097, Jul 2010.

[9] E. Aprile, K. Arisaka, F. Arneodo, A. Askin, L. Baudis, A. Behrens, K. Bokeloh, E. Brown, J. M. R. Cardoso, B. Choi, D. B. Cline, S. Fattori, A. D. Ferella, K.-L. Giboni, A. Kish, C. W. Lam, J. Lamblin, R. F. Lang, K. E. Lim, J. A. M. Lopes, T. Marrodán Undagoitia, Y. Mei, A. J. Melgarejo Fernandez, K. Ni, U. Oberlack, S. E. A. Orrigo, E. Pantic, G. Plante, A. C. C. Ribeiro, R. Santorelli, J. M. F. dos Santos, M. Schumann, P. Shagin, A. Teymourian, D. Thers, E. Tziaferi, H. Wang, and C. Weinheimer. First dark matter results from the xenon100 experiment. *Phys. Rev. Lett.*, 105(13):131302, Sep 2010.

[10] John P. Ralston. One Model Explains DAMA/LIBRA, CoGENT, CDMS, and XENON. arXiv preprint, 2010.

[11] A. Achterberg et al. Limits on the muon flux from neutralino annihilations at the center of the Earth with AMANDA. *Astropart.Phys.*, 26:129–139, 2006.

[12] Catherine De Clercq. Search for dark matter with the AMANDA and IceCube neutrino detectors (20'+5'). *PoS*, IDM2008:034, 2008.

[13] R. Trotta, R. Ruiz de Austri, and C. Perez de los Heros. Prospects for dark matter detection with IceCube in the context of the CMSSM. *JCAP*, 0908:034, 2009.

[14] T. Eberl. Status and first results of the ANTARES neutrino telescope. *Prog.Part.Nucl.Phys.*, 66:457–462, 2011.

[15] M. Ricci. The PAMELA satellite experiment: An observatory in space for particles, antiparticles and nuclei in the cosmic rays. *PoS*, BORMIO2010:047, 2010.

[16] E.A. Baltz, B. Berenji, G. Bertone, L. Bergstrom, E. Bloom, et al. Pre-launch estimates for GLAST sensitivity to Dark Matter annihilation signals. *JCAP*, 0807:013, 2008.

[17] S. Torii et al. High-energy electron observations by PPB-BETS flight in Antarctica. arXiv preprint, 2008.

[18] S.W. Barwick et al. Measurements of the cosmic ray positron fraction from 1-GeV to 50-GeV. *Astrophys.J.*, 482:L191–L194, 1997.

[19] J. et. al Chang. An excess of cosmic ray electrons at energies of 300 - 800 gev. *Nature*, 456, 2008.

[20] Alexander A. Andrianov, Domenec Espriu, Paola Giacconi, and Roberto Soldati. Anomalous positron excess from Lorentz-violating QED. *JHEP*, 0909:057, 2009.

[21] John McDonald. Enhanced Dark Matter Annihilation Rate for Positron and Electron Excesses from Q-ball Decay. *Phys.Rev.Lett.*, 103:151301, 2009.

[22] Dan Hooper, Pasquale Blasi, and Pasquale Dario Serpico. Pulsars as the Sources of High Energy Cosmic Ray Positrons. *JCAP*, 0901:025, 2009.

[23] Stefano Profumo. Dissecting Pamela (and ATIC) with Occam's Razor: existing, well-known Pulsars naturally account for the 'anomalous' Cosmic-Ray Electron and Positron Data. arXiv preprint, 2008.

[24] Dmitry Malyshev, Ilias Cholis, and Joseph Gelfand. Pulsars versus Dark Matter Interpretation of ATIC/PAMELA. *Phys.Rev.*, D80:063005, 2009. * Brief entry *.

[25] Hasan Yuksel, Matthew D. Kistler, and Todor Stanev. TeV Gamma Rays from Geminga and the Origin of the GeV Positron Excess. *Phys. Rev. Lett.*, 103:051101, 2009.

[26] Chuan-Ren Chen, Fuminobu Takahashi, and T.T. Yanagida. Gamma rays and positrons from a decaying hidden gauge boson. *Phys.Lett.*, B671:71–76, 2009.

[27] Peng-fei Yin, Qiang Yuan, Jia Liu, Juan Zhang, Xiao-jun Bi, et al. PAMELA data and leptonically decaying dark matter. *Phys.Rev.*, D79:023512, 2009.

[28] Alejandro Ibarra and David Tran. Decaying Dark Matter and the PAMELA Anomaly. *JCAP*, 0902:021, 2009.

[29] V. Barger, Y. Gao, Wai Yee Keung, D. Marfatia, and G. Shaughnessy. Dark matter and pulsar signals for Fermi LAT, PAMELA, ATIC, HESS and WMAP data. *Phys.Lett.*, B678:283–292, 2009.

[30] Xiao-Gang He. Dark Matter Annihilation Explanation for e+- Excesses in Cosmic Ray. *Mod.Phys.Lett.*, A24:2139–2160, 2009.

[31] Irit Maor. Annihilating dark matter and the galactic positron excess. arXiv preprint, 2006.

[32] Rouzbeh Allahverdi, Bhaskar Dutta, Katherine Richardson-McDaniel, and Yudi Santoso. A Supersymmetric B^- L Dark Matter Model and the Observed Anomalies in the Cosmic Rays. *Phys.Rev.*, D79:075005, 2009.

[33] Gert Huetsi, Andi Hektor, and Martti Raidal. Constraints on leptonically annihilating Dark Matter from reionization and extragalactic gamma background. *Astron.Astrophys.*, 505:999–1005, 2009. * Brief entry *.

[34] Maxim Pospelov and Adam Ritz. Astrophysical Signatures of Secluded Dark Matter. *Phys.Lett.*, B671:391–397, 2009.

[35] A. Abdo and Collaboration. Constraints on cosmological dark matter annihilation from the Fermi-LAT isotropic diffuse gamma-ray measurement. *JCAP*, 4:14–+, April 2010.

[36] Kim Griest and David Seckel. Three exceptions in the calculation of relic abundances. *Phys.Rev.*, D43:3191–3203, 1991.

[37] J. Alwal, M. Backovic, K.C. Kong, and M. McCaskey. Maddm, a madgraph extension for dark matter calculations. In preparation.

[38] T. Stelzer and W. F. Long. Automatic generation of tree level helicity amplitudes. *Comput. Phys. Commun.*, 81:357–371, 1994.

[39] Nima Arkani-Hamed, Douglas P. Finkbeiner, Tracy R. Slatyer, and Neal Weiner. A Theory of Dark Matter. *Phys.Rev.*, D79:015014, 2009.

[40] Junji Hisano, Shigeki. Matsumoto, Mihoko M. Nojiri, and Osamu Saito. Non-perturbative effect on dark matter annihilation and gamma ray signature from galactic center. *Phys.Rev.*, D71:063528, 2005.

[41] Edward W. Kolb and Michael S. Turner. The Early universe. *Front.Phys.*, 69:1–547, 1990.

[42] H. Rauch, M. Zawisky, Ch. Stellmach, and P. Geltenbort. Giant absorption cross section of ultracold neutrons in gadolinium. *Phys. Rev. Lett.*, 83(24):4955–4958, Dec 1999.

[43] Arno A. Penzias and Robert Woodrow Wilson. A Measurement of excess antenna temperature at 4080- Mc/s. *Astrophys. J.*, 142:419–421, 1965.

[44] A. A. Penzias and R. W. Wilson. Measurement of the Flux Density of CAS a at 4080 Mc/s. *"Astrophys. J."*, 142, oct 1965.

[45] George F. Smoot et al. Structure in the COBE differential microwave radiometer first year maps. *Astrophys. J.*, 396:L1–L5, 1992.

[46] Kingman Cheung and Tzu-Chiang Yuan. Hidden fermion as milli-charged dark matter in Stueckelberg Z' model. *JHEP*, 03:120, 2007.

[47] Jason Kumar and James D. Wells. CERN LHC and ILC probes of hidden-sector gauge bosons. *Phys.Rev.*, D74:115017, 2006.

[48] Tao Han, Zongguo Si, Kathryn M. Zurek, and Matthew J. Strassler. Phenomenology of hidden valleys at hadron colliders. *JHEP*, 0807:008, 2008.

[49] John March-Russell, Stephen M. West, Daniel Cumberbatch, and Dan Hooper. Heavy Dark Matter Through the Higgs Portal. *JHEP*, 0807:058, 2008.

[50] Pran Nath and Richard L. Arnowitt. Predictions in SU(5) supergravity grand unification with proton stability and relic density constraints. *Phys.Rev.Lett.*, 70:3696–3699, 1993.

[51] Subhaditya Bhattacharya, Utpal Chattopadhyay, Debajyoti Choudhury, Debottam Das, and Biswarup Mukhopadhyaya. Non-universal scalar mass scenario with Higgs funnel region of SUSY dark matter: A Signal-based analysis for the Large Hadron Collider. *Phys.Rev.*, D81:075009, 2010.

[52] William Shepherd, Tim M.P. Tait, and Gabrijela Zaharijas. Bound states of weakly interacting dark matter. *Phys.Rev.*, D79:055022, 2009.

[53] John David March-Russell and Stephen Mathew West. WIMPonium and Boost Factors for Indirect Dark Matter Detection. *Phys.Lett.*, B676:133–139, 2009. * Brief entry *.

[54] Mihailo Backovic and John P. Ralston. Limits on Threshold and 'Sommerfeld' Enhancements in Dark Matter Annihilation. *Phys.Rev.*, D81:056002, 2010.

[55] Junji Hisano, Shigeki Matsumoto, and Mihoko M. Nojiri. Explosive dark matter annihilation. *Phys.Rev.Lett.*, 92:031303, 2004.

[56] S. Orito et al. Precision measurement of cosmic-ray antiproton spectrum. *Phys. Rev. Lett.*, 84:1078–1081, 2000.

[57] M. Boezio et al. The cosmic-ray anti-proton flux between 3-GeV and 49- GeV. *Astrophys. J.*, 561:787–799, 2001.

[58] Stephane Coutu et al. Cosmic-ray positrons: Are there primary sources? *Astropart. Phys.*, 11:429–435, 1999.

[59] John F. Beacom, Nicole F. Bell, and Gregory D. Mack. General Upper Bound on the Dark Matter Total Annihilation Cross Section. *Phys.Rev.Lett.*, 99:231301, 2007.

[60] Masahiro Ibe, Hitoshi Murayama, and T.T. Yanagida. Breit-Wigner Enhancement of Dark Matter Annihilation. *Phys.Rev.*, D79:095009, 2009.

[61] Wan-Lei Guo and Yue-Liang Wu. Enhancement of Dark Matter Annihilation via Breit-Wigner Resonance. *Phys.Rev.*, D79:055012, 2009.

[62] Paulo F. Bedaque, Michael I. Buchoff, and Rashmish K. Mishra. Sommerfeld enhancement from Goldstone pseudo-scalar exchange. *JHEP*, 0911:046, 2009.

[63] Massimiliano Lattanzi and Joseph I. Silk. Can the WIMP annihilation boost factor be boosted by the Sommerfeld enhancement? *Phys.Rev.*, D79:083523, 2009. * Brief entry *.

[64] Kimball A. Milton and Igor L. Solovtsov. Relativistic Coulomb resummation in QCD. *Mod.Phys.Lett.*, A16:2213–2220, 2001.

[65] S.J. Brodsky, A.H. Hoang, Johann H. Kuhn, and T. Teubner. Angular distributions of massive quarks and leptons close to threshold. *Phys.Lett.*, B359:355–361, 1995.

[66] Roberto Iengo. Sommerfeld enhancement for a Yukawa potential. arXiv preprint, 2009.

[67] E. Guth and C. J. Mullin. Momentum representation of the coulomb scattering wave functions. *Phys. Rev.*, 83(3):667–668, Aug 1951.

[68] Isadore Harris and Laurie M. Brown. Radiative corrections to pair annihilation. *Phys. Rev.*, 105(5):1656–1661, Mar 1957.

[69] G. Elwert. Verschaerfte berechnung von intensitaet und polarisation in kontinuierlichen roentgenspektrum. *Annalen der Physik*, 34:178, 1939.

[70] G. Elwert and E. Haug. Calculation of bremsshtrahlung cross sections with sommerfeld-maue eigenfunctions. *Physical Review*, 183:90, 1969.

[71] Eugene Guth. Radiative transition probabilities in heavy nuclei. excitation of nuclei by x-rays. *Phys. Rev.*, 59(4):325–331, Feb 1941.

[72] R. H. Pratt and H. K. Tseng. Tip region of the bremsstrahlung spectrum from incident electrons of kinetic energy 50 keV—1.84 MeV. *Phys. Rev. A*, 11(6):1797–1803, Jun 1975.

[73] Lam Hui. Unitarity bounds and the cuspy halo problem. *Phys.Rev.Lett.*, 86:3467–3470, 2001.

[74] Eugene P. Wigner. On the behavior of cross sections near thresholds. *Phys. Rev.*, 73(9):1002–1009, May 1948.